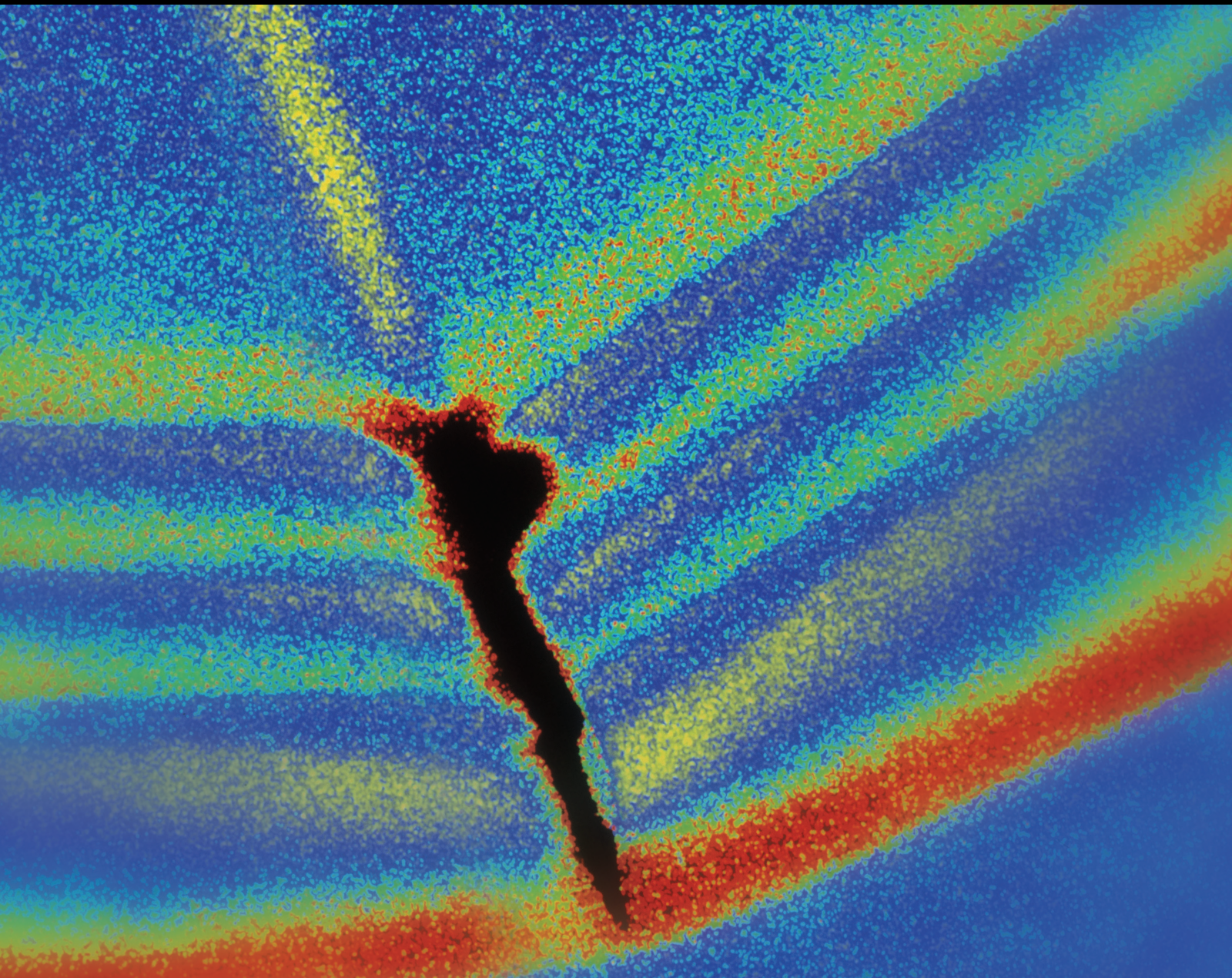# Advances in Early-stage Novelty Inspection and Structural Condition Assessment

Lead Guest Editor: Yun-Lai Zhou
Guest Editors: Eloi Figueiredo, Linya Liu, Xianying Zhang, and Weiji Liu

Advances in Early-stage Novelty Inspection and Structural Condition Assessment

Advances in Early-stage Novelty Inspection and Structural Condition Assessment

Lead Guest Editor: Yun-Lai Zhou
Guest Editors: Eloi Figueiredo, Linya Liu, Xianying Zhang, and Weiji Liu
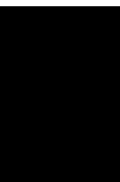
Amal Hajjaj, United Kingdom
Mohammad A. Hariri-Ardebili, USA
Seyed M. Hashemi, Canada
Xue-qiu He, China
Agustin Herrera-May, Mexico
M.I. Herreros, Spain
Duc-Duy Ho, Vietnam
Hamid Hosano, Japan
Jin Huang, China
Ahmed Ibrahim, USA
Bernard W. Ikua, Kenya
Xingxing Jiang, China
Jiang Jin, China
Xiaohang Jin, China
MOUSTAFA KASSEM, Malaysia
Shao-Bo Kang, China
Yuri S. Karinski, Israel
Andrzej Katunin, Poland
Manoj Khandelwal, Australia
Denise-Penelope Kontoni, Greece
Mohammadreza Koopialipoor, Iran
Georges Kouroussis, Belgium
Genadijus Kulvietis, Lithuania
Pradeep Kundu, USA
Luca Landi, Italy
Moon G. Lee, Republic of Korea
Trupti Ranjan Lenka, India
Arcanjo Lenzi, Brazil
Marco Lepidi, Italy
Jinhua Li, China
Shuang Li, China
Zhixiong Li, China
Xihui Liang, Canada
Tzu-Kang Lin, Taiwan
Jinxin Liu, China
Ruonan Liu, China
Xiuquan Liu, China
Siliang Lu, China
Yixiang Lu, China
R. Luo, China
Tianshou Ma, China
Nuno M. Maia, Portugal
Abdollah Malekjafarian, Ireland
Stefano Manzoni, Italy

Stefano Marchesiello, Italy
Francesco S. Marulo, Italy
Traian Mazilu, Romania
Vittorio Memmolo, Italy
Jean-Mathieu Mencik, France
Laurent Mevel, France
Letícia Fleck Fadel Miguel, Brazil
FuRen Ming, China
Fabio Minghini, Italy
Marco Miniaci, USA
Mahdi Mohammadpour, United Kingdom
Rui Moreira, Portugal
Emiliano Mucchi, Italy
Peter Múčka, Slovakia
Fehmi Najar, Tunisia
M. Z. Naser, USA
Amr A. Nassr, Egypt
Sundararajan Natarajan, India
Toshiaki Natsuki, Japan
Miguel Neves, Portugal
Sy Dzung Nguyen, Republic of Korea
Trung Nguyen-Thoi, Vietnam
Gianni Niccolini, Italy
Rodrigo Nicoletti, Brazil
Bin Niu, China
Leilei Niu, China
Yan Niu, China
Lucio Olivares, Italy
Erkan Oterkus, United Kingdom
Roberto Palma, Spain
Junhong Park, Republic of Korea
Francesco Pellicano, Italy
Paolo Pennacchi, Italy
Giuseppe Petrone, Italy
Evgeny Petrov, United Kingdom
Franck Poisson, France
Luca Pugi, Italy
Yi Qin, China
Virginio Quaglini, Italy
Mohammad Rafiee, Canada
Carlo Rainieri, Italy
Vasudevan Rajamohan, India
Ricardo A. Ramirez-Mendoza, Mexico
José J. Rangel-Magdaleno, Mexico

Didier Rémond, France
Dario Richiedei, Italy
Fabio Rizzo, Italy
Carlo Rosso, Italy
Riccardo Rubini, Italy
Salvatore Russo, Italy
Giuseppe Ruta, Italy
Edoardo Sabbioni, Italy
Pouyan Roodgar Saffari, Iran
Filippo Santucci de Magistris, Italy
Fabrizio Scozzese, Italy
Abdullah Seçgin, Turkey
Roger Serra, France
S. Mahdi Seyed-Kolbadi, Iran
Yujie Shen, China
Bao-Jun Shi, China
Chengzhi Shi, USA
Gerardo Silva-Navarro, Mexico
Marcos Silveira, Brazil
Kumar V. Singh, USA
Jean-Jacques Sinou, France
Isabelle Sochet, France
Alba Sofi, Italy
Jussi Sopanen, Finland
Stefano Sorace, Italy
Andrea Spaggiari, Italy
Lei Su, China
Shuaishuai Sun, Australia
Fidelis Tawiah Suorineni, Kazakhstan
Cecilia Surace, Italy
Tomasz Szolc, Poland
Iacopo Tamellin, Italy
Zhuhua Tan, China
Gang Tang, China
Chao Tao, China
Tianyou Tao, China
Marco Tarabini, Italy
Hamid Toopchi-Nezhad, Iran
Carlo Trigona, Italy
Federica Tubino, Italy
Nerio Tullini, Italy
Nicolò Vaiana, Italy
Marcello Vanali, Italy
Christian Vanhille, Spain

Dr. Govind Vashishtha, Poland
F. Viadero, Spain
M. Ahmer Wadee, United Kingdom
C. M. Wang, Australia
Gaoxin Wang, China
Huiqi Wang, China
Pengfei Wang, China
Weiqiang Wang, Australia
Xian-Bo Wang, China
YuRen Wang, China
Wai-on Wong, Hong Kong
Yuanping XU, China
Biao Xiang, China
Qilong Xue, China
Xin Xue, China
Diansen Yang, China
Jie Yang, Australia
Chang-Ping Yi, Sweden
Nicolo Zampieri, Italy
Chao-Ping Zang, China
Enrico Zappino, Italy
Guo-Qing Zhang, China
Shaojian Zhang, China
Yongfang Zhang, China
Yaobing Zhao, China
Zhipeng Zhao, Japan
Changjie Zheng, China
Chuanbo Zhou, China
Hongwei Zhou, China
Hongyuan Zhou, China
Jiaxi Zhou, China
Yunlai Zhou, China
Radoslaw Zimroz, Poland

Contents

Research Article

Stochastic Damage Constitutive Relationship of Steel-Reinforced Concrete Bond-Slip

Ming Xie [ID],[1,2] **Jiahao Liu**,[1,2] **Peng Wang**,[1,2] **Zi Wang**,[1,2] **and Jingjing Zhou**[1,2]

[1]*School of Civil Engineering, Xijing University, Xi'an 710123, Shaanxi, China*
[2]*Shaanxi Key Laboratory of Safety and Durability of Concrete Structures, Xijing University, Xi'an 710123, Shaanxi, China*

Correspondence should be addressed to Ming Xie; 20170223@xijing.edu.cn

The bond-slip damage of the interface between profile steel and concrete is the key point of steel-reinforced concrete structure. This paper is based on the statistical analysis of a large amount of experimental data and the distribution characteristics of bonding stress on the bonding surface of the profile steel and concrete, and the conversion rules between the three parts (chemical bonding force, frictional resistance, and mechanical interaction) of the bond force are obtained. According to the mutual conversion rules of the three parts of the bonding force on the steel-reinforced concrete bonding surface, a mesomechanical model based on the spring-friction block element is established. Taking into account the discreteness of concrete performance on the bonding surface and the randomness of defects, using the stochastic damage theory, a constitutive model of stochastic bonding damage on the steel-reinforced concrete bonding surface is established. The comparative analysis with the results of a large number of steel-reinforced concrete pull-out tests shows that the model can reasonably reflect the damage characteristics of the steel-reinforced concrete bonding surface.

1. Introduction

The steel-reinforced concrete structures have been widely used in practical engineering due to their excellent durability, economical advantage, and antiseismic performance. The experimental research shows that there is a bond-slip problem between profile steel and concrete in steel-reinforced concrete structures, and the bond-slip problem has a significant adverse effect on the working performance of the steel-reinforced concrete structure [1–12]. At present, domestic and foreign scholars have made many achievements in the design and calculation theory of steel-reinforced concrete, but there are still many problems that have not yet reached a consensus. In particular, the bond-slip problem between profile steel and concrete is usually simplified or ignored in the calculation and analysis of steel-reinforced concrete structures. When studying the damage of steel-reinforced concrete structures, the international scholars pay more attention to the study of damage effects on concrete performance, while the bonding damage of the interface between profile steel and concrete is neglected.

Based on the bond-slip properties of steel-reinforced concrete interface, the study of the bonding damage mechanism of steel-reinforced concrete interface will provide an important theoretical basis for the study of the damage performance of steel-reinforced concrete structures. However, concrete is a multicomponent, multiphase, and heterogeneous composite material; its internal constituent structure includes cement stone, aggregates of different shapes and sizes, and various capillaries (void structures) formed during the concrete preparation process [13], so the mechanical properties of concrete have obvious discreteness and randomness. Based on the study of bond-slip properties of steel-reinforced concrete interface, the randomness of concrete material properties is considered, a stochastic damage model based on the mesomechanical model of steel-reinforced concrete interface is established to extend the deterministic constitutive model to the probabilistic version. The structural relationship objectively reflects the nondeterminism of the mechanical properties of steel-reinforced concrete materials under different stress stages and provides

a reference for the establishment of damage constitutive relations of steel-reinforced concrete under complex stress conditions.

2. Damage Model and Damage Index Definition

2.1. Analysis on Bonding Stress.
The bonding force between profile steel and concrete is the key to ensure that the profile steel works with concrete. The bonding force between profile steel and concrete is mainly consisted of three parts: chemical bonding force, frictional resistance, and mechanical interaction. Researches have shown that the chemical bonding force exists only in the original forming state of members. Once the bond-slip on the joint surface between profile steel and concrete occurs, the cement crystal will be sheared and crushed, and the chemical bonding force will be lost and converted into frictional resistance and mechanical interaction [10]. At the same time, the chemical bonding force will be generated within the diffusion length of the chemical bonding force that has not yet slipped, so that the frictional resistance, the mechanical interaction, and the chemical bonding force of the nonslip section can constitute a new force to jointly bear the external load and achieve a new balance (Figure 1).

2.2. Mesomechanical Model.
According to the characteristics of the above-mentioned steel-reinforced concrete interface bonding, the spring-friction block model of J. Eeibl is introduced to simulate the force of the interface [14] (Figures 2 and 3). In Figure 2, the steel-reinforced concrete bonding surface of the steel-reinforced concrete pull-out test can be simulated by numerous spring-friction block elements as shown in Figure 3. Assume that the profile steel and concrete outside the bonding surface are rigid; consider only the force on the bonding surface, not the deformation of the profile steel and concrete, and then the external force of each spring-friction block element on the bonding surface is unified.

2.3. Analysis of Microscopic Element Mechanism.
As shown in Figure 4, the spring and the friction block are connected in parallel, and the slip controller limits the slip starting position of the friction block, so that the friction block does not slip before the spring is broken. P_1 is the external force borne by the spring in the spring-friction block element, P_f is the external force borne by the friction block in the spring-friction block element, and $P_1 = P_f (\Delta < \Delta_0)$ or $P_f = P (\Delta \geq \Delta_0)$. Δ_e is the tensile displacement of the spring, Δ_d is the sliding displacement of the friction block, and $\Delta_e = S$ ($S < S_0$) or $\Delta_d = S - S_0$ ($S \geq S_0$). As shown in Figure 5, the left graph shows the load-displacement curve of the spring and the friction block, and the right graph shows the overall load-displacement curve of the spring-friction block element. $P_0 f$ is the sliding friction resistance of the friction block, Δ_m is the ultimate sliding displacement of the friction block, and Δ_0 is the ultimate tensile displacement of the spring. Only the spring is stressed when the slip of the bonding surface is less than the ultimate displacement Δ_0 of the spring, and the load-displacement curve is an oblique straight line (from point 0 to point A); meanwhile the spring is broken when the slip is greater than or equal to the ultimate displacement Δ_0 of the spring. It may be assumed that the maximum static friction force of the friction block is less than or equal to the ultimate bearing capacity of the spring, and then the friction block begins to slide, generating sliding friction, and its load-displacement curve is a horizontal straight line (from point A to point B).

When the slippage of the bonding surface S is less than the ultimate displacement Δ_0 of the spring, the load on the steel-reinforced concrete interface is borne by the chemical bonding force, there is no frictional resistance or mechanical interaction, and the frictional resistance does not slip relatively; when the slip is equal to the ultimate displacement Δ_0, the chemical bonding force disappears, the spring breaks, the load on the steel-reinforced concrete interface begins to be borne by the mechanical interaction and the friction resistance, and the friction blocks begin to slip relatively to each other and produce sliding friction; when the amount of slip continues to increase, due to the fact that the sliding friction remains unchanged and the spring-friction block elements cannot resist the continuous increase of external load, the adjacent spring-friction block elements will participate in the force in turn; when the slippage reaches the ultimate displacement Δ_m of the friction block, the friction block falls off, the frictional resistance and the mechanical interaction are lost, and the spring-friction block element is completely broken; when all spring-friction block elements on the bonding surface are broken, the bonding surface is completely destroyed.

2.4. Definition of Damage Index.
Assume that the interface damage of steel-reinforced concrete follows the continuum damage mechanics, and the interface damage variable is defined as the ratio of the fractured area to the total area; that is,

$$D = \frac{A_\omega (S)}{A}, \tag{1}$$

where A_ω is the damage area, that is, the area of the fractured interface; A is the original area, that is, the total bonded area of profile steel and concrete.

For the spring element, the damage area defined on the bonding surface is

$$A_\omega (S) = \sum_{i=1}^{Q} H (S - \Delta_{0i}) dA_i, \tag{2}$$

where A_i is the cross-sectional area of the i-th spring element; Q is the total number of spring elements on the original bonding surface; Δ_{0i} is the ultimate tensile displacement of the i-th spring, that is, Δ_0 of the i-th spring.

$H(x)$ is Heaviside equation; that is,

$$H (S - \Delta_i) = \begin{cases} 0, & S \leq \Delta_{0i}, \\ 1, & S > \Delta_{0i}. \end{cases} \tag{3}$$

Substituting equation (2) into equation (1), the damage variable $D(S)$ of the spring element can be obtained as

Concrete

Shaped steel

A: Bond-slip zone B_1: Damaged concrete
C: Chemical adhering zone B_2: Damage transition layer
D: Non-bonded stress zone

Concrete

Shaped steel

Chemical bonding force

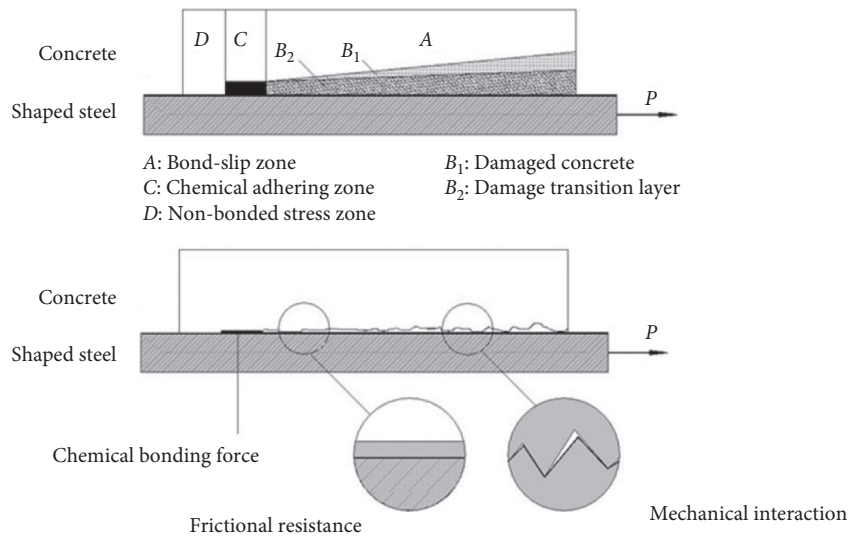Frictional resistance   Mechanical interaction

FIGURE 1: Sketch of the bonding stress distribution.
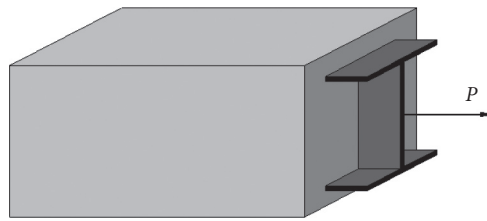
FIGURE 2: Steel-reinforced concrete pull-out test.

Concrete

Shaped steel
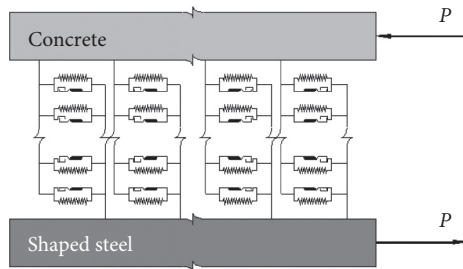
FIGURE 3: Spring-friction block equivalent model.

Spring $P_1 \Delta_e$

Friction
block $P_f \Delta_d$

Slip controller Δ_0
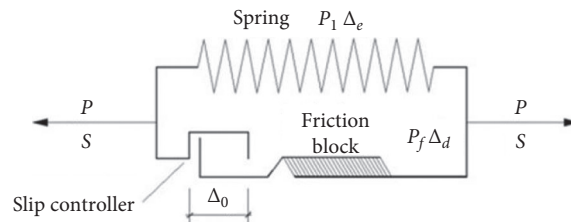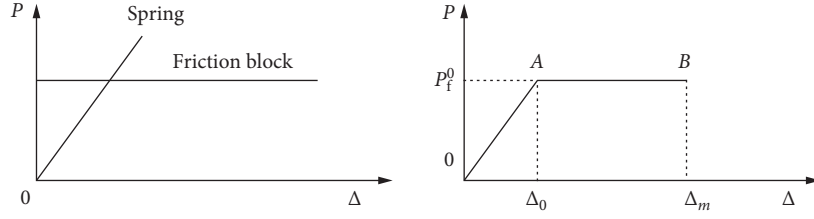
FIGURE 4: Spring-friction block microelement.

FIGURE 5: Load-displacement relationship of spring-friction block element.

$$D(S) = \frac{A_\omega(S)}{A},$$

$$= \frac{1}{A} \sum_{i=1}^{Q} H(S - \Delta_{0i}) dA_i,$$

$$= \frac{1}{A} \int_0^1 H(S - \Delta(x)) \mathrm{d}(x), \qquad (4)$$

$$= \int_0^1 H\left(S - \Delta\left(\frac{x}{A}\right)\right) \mathrm{d}\left(\frac{x}{A}\right),$$

$$= \int_0^1 H(S - \Delta(y)) \mathrm{d}(y),$$

where $\Delta(x)$ is the ultimate deformation of the spring element along the direction of the external force; $\Delta(y)$ is the ultimate deformation of the spring element on section y at x.

Similarly, the damage index of the friction block element on the bonding surface can be defined as $D_f(S)$:

$$D_f(S) = \frac{A_\omega^f(S)}{A},$$

$$= \frac{1}{A} \sum_{i=1}^{Q} H(S - \Delta_{mi}) dA_i, \qquad (5)$$

$$= \int_0^1 H(S - \Delta(z)) \mathrm{d}(z),$$

where $Af\omega$ is the damage area defined by the friction block element, that is, the area of the adhesive surface where the friction block has fallen off; Δ_{mi} is the ultimate sliding displacement of the i-th friction block, that is, Δ_m of the i-th friction block; $\Delta(z)$ is ultimate deformation of the friction block element on the section along the external force direction z.

According to the stochastic damage theory, the spring stiffness on the bonding surface of profile steel and concrete and the friction coefficient of the friction block should be stochastic, but doing this will result in very complex subsequent calculations. To simplify the calculation, it may be assumed that the spring stiffness and friction coefficient of friction block in all spring-friction block elements on the bonding surface are constant, and the ultimate deformation of the spring and friction block is considered as a stochastic variable; we also assume that $\Delta(z)$ and $\Delta(y)$ are stochastic variables that follow the same rules of distribution, so the spring damage index $D(S)$ and the friction block stochastic

index $D_f(S)$ are also stochastic variables that follow the same rules of distribution.

3. Stochastic Damage Constitutive Relation

3.1. Mesomechanical Model Failure Mode. The damage process of the bonding interface mesomechanical model is divided into four stages: no damage stage, elastic damage stage, plastic damage stage, and complete damage stage (Figure 6). In the no damage stage, the external force is less than or equal to the ultimate bearing capacity of the spring, the external force is entirely borne by the spring, the friction block has no relative slip, and work $W_p(S)$ done by the external force is all converted by the spring into elastic internal energy $W_e(S)$. As the load continues to increase, due to $\Delta(y)$ being a stochastic variable, the spring begins to rupture at the smaller point where $\Delta(y)$ is smaller, and the mesomechanical model enters the elastic damage stage. At this time, the external force work corresponding to the broken part of the spring is transformed into the spring breaking energy $W_d(S)$. After the spring is broken, the corresponding external force is borne by the friction block, and the model enters the plastic damage stage. At this stage, the friction block produces relative slip. When the external force is constant, the bond-slip continues to increase. Due to the fact that both $\Delta(z)$ and $\Delta(y)$ are stochastic variables, the friction block begins to fall off at the smaller part of $\Delta(z)$. The work of external forces is partly converted by friction into internal energy and partly into the fracture energy of the friction block. With the further increase of the slippage, the damaged area of the spring and friction block continues to increase, until all springs and friction blocks on the entire bonding surface are destroyed, and the model enters the stage of complete damage. It can be seen that the external force is converted into the elastic potential energy which is stored and the fracture potential energy is consumed.

3.2. Stochastic Damage Constitutive Relation. Based on the above analysis of the failure mode of the bond-slip mesomechanical model of the steel-reinforced concrete interface, according to the law of conservation of energy, the energy balance equation can be obtained as

$$\begin{cases} W_P(S) = W_e(S), & S < S_0, \\ W_P(S) = W_e(S) - W_d(S), & S \geq S_0. \end{cases} \qquad (6)$$

In equation (6),
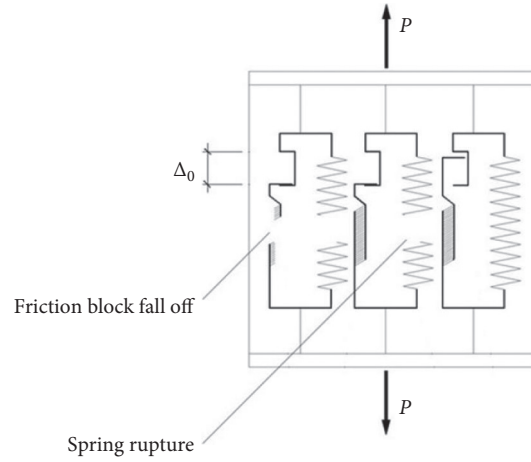
Figure 6: Model failure mode.

$$
\begin{cases}
W_e(S) = \Delta_e P_1, \\[2ex]
\quad = SP, \\[2ex]
\quad = \dfrac{1}{2} ES^2 \quad S < S_0, \\[2ex]
W_e(S) = \Delta_e P_1 + \Delta_d P_f, \\[2ex]
\quad = SP + (S - S_0)P_f^0, \\[2ex]
\quad = \dfrac{1}{2} ES^2 + \dfrac{1}{A} \displaystyle\int_{S_0}^{S} P_f^0 \lim_{Q \to \infty} \sum_{i=1}^{Q} H(S - \Delta_{0i}) A_i dx, \\[2ex]
\quad = \dfrac{1}{2} ES^2 + \displaystyle\int_{S_0}^{S} P_f^0 D(x) dx \quad S \geq S_0,
\end{cases}
\tag{7}
$$

$$
\begin{aligned}
W_d(S) &= \frac{1}{A} \int_{S_0}^{S} \lim_{Q \to \infty} \sum_{i=1}^{Q} ExH(S - \Delta_i) A_i dx + \int_{S_0}^{S} P_f^0 \frac{1}{A} \lim_{Q \to \infty} \sum_{i=1}^{Q} H(S - \Delta_i) A_i dx \frac{1}{A} \lim_{Q \to \infty} \sum_{i=1}^{Q} H(S - \Delta_i) A_i dx, \\
&= \int_{S_0}^{S} ExD(x) dx + \int_{S_0}^{S} P_f^0 D(x) D_f(x) dx
\end{aligned}
\tag{8}
$$

Substituting equation (7) and equation (8) into equation (6), the following can be obtained:

$$
\begin{cases}
\displaystyle\int_{0}^{S} P(x) dx = \dfrac{1}{2} ES^2 \quad S < S_0, \\[3ex]
\displaystyle\int_{S_0}^{S} P(x) dx = \dfrac{1}{2} ES^2 + \int_{S_0}^{S} P_f^0 D(x) dx - \int_{S_0}^{S} ExD(x) dx - \int_{S_0}^{S} P_f^0 D(x) D_f(x) dx \quad S \geq S_0.
\end{cases}
\tag{9}
$$

The derivative of S in equation (9) is

$$\begin{cases} P(S) = ES, & S < S_0, \\ P(S) = ES - ESD(S) + P_f^0 D(S) - P_f^0 D(S) D_f(S), \\ \quad = ES[1 - D(S)] + P_f^0 D(S)[1 - D_f(S)], \\ \quad = ES[1 - D(S)] + E_0 S_0 D(S)[1 - D_f(S)] & S \geq S_0. \end{cases}$$
(10)

Equation (10) is the stochastic damage constitutive relationship of the bonding surface between profile steel and concrete. When the slippage is less than S_0, the bonding surface is in the elastic phase without damage; when the deformation is greater than or equal to S_0, the bonding surface begins to be damaged, and $S_0 = \min (\Delta_{0i})$.

Studies have shown that the microscopic defects and congenital damage of concrete follow the lognormal distribution [12]. Therefore, it is assumed that the damage index and stiffness of the profile steel and concrete bonding surface are subject to lognormal distribution; that is, $\log D \sim (\mu_d, \sigma2\ d)$ and $\log E \sim (\mu_e, \sigma2\ e)$.

Then the average form of equation (10) can be written as

$$\begin{cases} \mu_\sigma(S) = \mu_E S, & S < S_0, \\ \mu_\sigma(S) = \mu_E S[1 - \mu_D(S)] + \mu_{E_0} S_0 \mu_D(S)[1 - \mu_{D_f}(S)], & S \geq S_0. \end{cases}$$
(11)

Similarly, its variance form can be written as

$$\begin{cases} \mathrm{var}P(S) = S^2 \sigma_E^2, & S < S_0, \\ \mathrm{var}P(S) = S^2\left(\sigma_E^2 - \sigma_E^2 \sigma_D^2 - \sigma_E^2 \mu_D^2 - \sigma_D^2 \mu_E^2\right) + \mu_{E_0}^2 S_0^2\left(2\sigma_D^2 + \mu_D^2 + \sigma_D^2 \sigma_D^2 \sigma_{D_f}^2 + 2\mu_D^2 \sigma_{D_f}^2 + 2\sigma_D^2 \mu_{D_f}^2 + \mu_D^2 \mu_{D_f}^2\right), & S \geq S_0. \end{cases}$$
(12)

4. Experimental Research

To verify the accuracy of the damage model established in this paper, the pull-out test data of medium-sized steel-reinforced concrete in the literature [3] are compared with the numerical calculation results of the model.

4.1. Design and Production of Test Pieces. The experimental design of this paper is mainly based on the axial pull-out test (as shown in Figure 7). All profile steels used in the test pieces are made of two I-channel steel and two 6 mm thick steel plates (Figure 8) to embed the resistance strain gauges in the flanges and webs (longitudinal) (measuring the longitudinal bonding stress of the flange and the web, as well as the distribution along the anchor length). Production of the combined I-beam and arrangement of embedded measuring points is as follows: ① On the web of one of the two channel steel plates and in the middle of one of the two bonded steel plates, a 3 mm × 15 mm longitudinal through length groove is precisely by a milling machine, and a circular hole with a diameter of 6 *mm* is drilled longitudinally along the middle of the other ungrooved channel steel plates and the steel plates according to certain spacing requirements (from dense to thin) (for embedding slip sensors). ② Use a momentary strong adhesive (T-1 502 glue) to longitudinally paste the resistance strain gauge from dense to sparse according to certain spacing requirements (depending on the embedded length of the steel used for the test piece, the groove steel web, and the upper and lower flange steel plates, each patch is 8~12 pieces); after the insulation piece is insulated and moisture-proof, it is taken out from two ends of the groove through the connecting wire, and then the groove is filled, compacted, and smoothed with epoxy resin, the groove is made with acetone, and the steel surface outside the groove is cleaned with acetone. ③ After the epoxy resin is substantially solidified, the ungrooved channel steel and the corresponding grooved buried resistance strained channel steel are bonded into the I-beam by epoxy resin glue, and the two channel steels are tightly coupled and uniformly pressed for a certain time. To avoid the epoxy resin glue in the construction to block the reserved hole on the ungrooved steel web, the hole on the bonding side of the channel is protected with a tape in advance, and the clay is filled in the hole. ④ After the two channels of steel are firmly bonded, the outer surface of the flange is cleaned with acetone. Then, two corresponding lengths of steel plate, respectively, adhere to the outside of the two flanges of the combined channel steel by epoxy glue and put pressure on it evenly for a certain time to make it tightly bound. ⑤ After the outer steel plate of the flange is firmly bonded, the combined I-steel surface is thoroughly cleaned with acetone, and a slip sensor is installed on its flange and webs (Figure 8).

Geometry and section size of the I-beam are as follows: depth of section $h_a = 112$ mm; flange width $b_f = 96$ mm; flange thickness $t_f = 14.5$ mm; web thickness $t_w = 10.6$ mm; web height $h_w = 83$ mm; sectional area $A_s = 3602$ mm^2; flange and web surface area $A_f = 835$ mm^2 and $A_w = 2767$ mm^2; perimeter $C_s = 572$ mm.

To understand the bond-slip mechanism, the main influencing factors, the distribution of bonding stress, and slip along the anchor length, four factors of the tensile test need to be considered comprehensively: concrete strength grade (f_c), concrete protective layer thickness (c), steel anchor length (l_0), and transverse hoop ratio (ρ_{sv}). According to the orthogonal test design principle, each factor considers 4 levels of design (regardless of the orthogonal conditions of interaction), and a total of 16 test pieces were designed.

The concrete of the test piece is based on the design strength grade, refers to the relevant provisions of the "Concrete and Reinforced Concrete Construction Manual," and combines them with the relevant research results of the Building Engineering Materials Testing and Testing Center
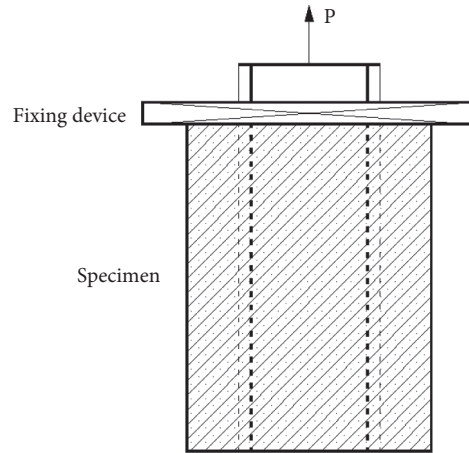
FIGURE 7: Schematic diagram of steel-reinforced concrete extraction test.
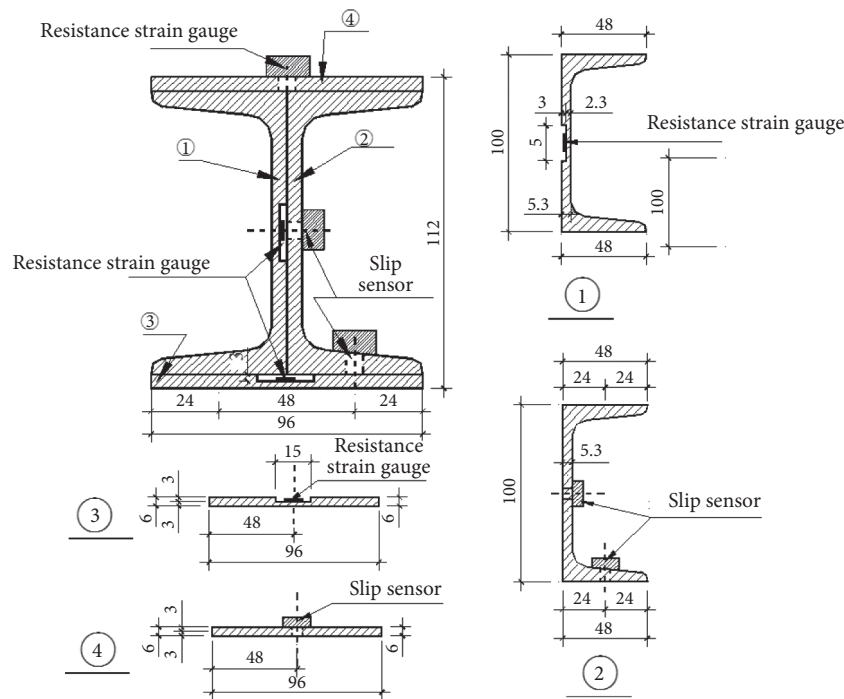
FIGURE 8: Steel combination I-beam.

of Xidian University. The main materials for making concrete specimens are Qinling cement, Weihe sand, gravel (the diameter is 5~8 mm), and tap water.

The concrete is manually mixed and mechanically vibrated and poured evenly in batches at one time (make 4 thumps every day), and damaging the slip sensors and strain measuring points arranged on the embedded steel flanges and webs of the test piece is avoided as much as possible, and the vibrating place is strictly controlled during vibrating. At the same time as the specimen is poured, each batch of test pieces is made 3 cube strength test blocks $(150 \times 150 \times 150 \, \text{mm}^3)$ in the same batch of concrete. These test blocks and the test pieces were maintained under the same conditions for 28 days. According to the standard test method, unidirectional axial compression tests are carried

out on the reserved concrete test block, and its relevant mechanical performance indexes are obtained. To protect the embedded profile steel with a slip sensor, the test piece adopts horizontal pouring concrete (as is shown in Figures 9 and 10).

The parameters for pulling out test pieces are listed in Table 1. The test pieces of interior steel are as follows: Φ16 (HRB335) for the main rib, Φ6 (HPB235) and Φ8 (HPB235) for the stirrup, and Q235 for both the steel plate and the channel steel. According to the metal tensile test method (GB228-87), the mechanical properties of the steel are tested.

4.2. Test Loading Scheme. The test is carried out in the Seismic Structure Laboratory of Xi'an University of Architecture and Technology. The loading devices used were a
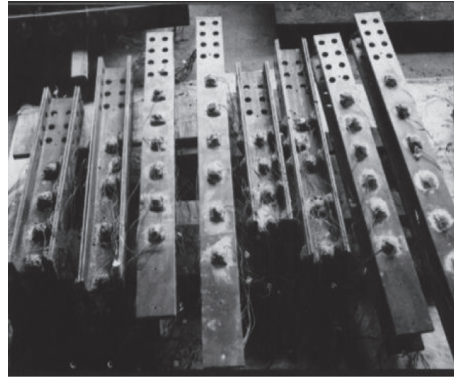
Figure 9: The embedded profile steel with strain and slip detection points has been set.
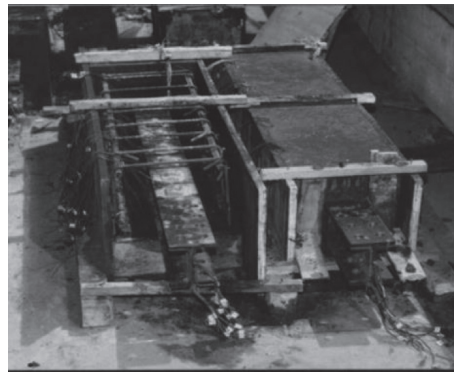
Figure 10: Forming and pouring test pieces.

100-ton pseudohydrostatic servo actuator and a 5000 kN long column tester, where the former is used for shaft pull-out and push-pull repeated loading tests and the latter for shaft push and short column tests.

The lower end of the test piece is free, and the upper end is the load end. The full section of the upper concrete is fixed by the steel plate (thickness of 40 mm), the beam, and the gantry device. The pull-out force is applied to the embedded steel and is transmitted from the steel to the concrete through the bonding between the steel and the concrete. The bonding stress between the steel and concrete and its relative slip occur at the loading end (upper end) of the test piece and gradually develop along the anchor length with the pull-out force increasing. This loading mode is similar to the stress state of the tension zone of the steel-reinforced concrete beam column.

The load used in the test is vertical static load, and the loading mode is monotonic axial load and repeated axial load. To avoid eccentricity during the test, physical alignment is carried out in a professional manner: the electronic dial gauges are placed symmetrically on both sides of the middle part of the specimen; by preloading and adjusting the loading device until the reading of the 2,000 measuring instruments is close, the basic alignment is considered.

Axial pull-out loading program is as follows: loading 2 tons per stage before the loading end of the test piece starts to slip and loading 1 ton per stage after the slip occurs. When the sliding reaches about 5 mm, the load tends to be stable,

adopting the displacement of 2 mm or 4 mm which is controlled to be loaded until the steel is pulled out by about 200 mm. The proposed load and displacement are controlled by the hydraulic servo control system in a timely manner, monitored, and recorded online by a computer. This loading method can fully develop the slip between profile steel and concrete, so that the bonding splitting failure shape of the steel-reinforced concrete member is more apparent.

Axial launch and short column loading procedure is as follows: Load at 2 tons or 2.5 tons per stage, stabilize the data for about 2 minutes after reaching intended load, and then record the data and carry out the next level of loading until the ultimate load is reached. The intended load is directly controlled by the dial of the testing machine, monitored, and recorded by the computer at the right time. The test includes the bond load on the specimen, the relative slip strains of reinforcement and concrete at the loaded and free ends, the profile steel and its distribution along the anchor length, the distribution of relative slip of the reinforcement and concrete at the joint surface, and the crack width.

Measurement of end bond-slip is as follows: Electronic dial indicators (or dial indicators) are installed at the 4 corners of the loading end and the free end of the specimen to directly measure the relative slip value at the 4 corners of the end section which can be directly measured and the average value of the 4 tables can be used as the end bond-slip value. The data measured by the electronic dial indicator (or

TABLE 1: List of parameters for pulling out test pieces.

Test piece number	Concrete strength f_{cu} (N/mm²)	Protective cover thickness C_a (mm)	Sectional dimension (mm²)	Steel buried depth l_a (mm)	Hoop form	Stirrup reinforcement ratio ρ_{sv} (%)	The ratio of longitudinal reinforcement ρ_s (%)	Steel ratio ρ_a (%)
A-1 (1)	C60	40	180 × 200	340	Φ6@180	0.18	3.35	10.01
A-2 (2)	C60	60	220 × 240	540	Φ8@100	0.26	2.29	6.82
A-3 (3)	C60	80	260 × 280	740	Φ8@115	0.34	1.66	4.95
A-4 (4)	C60	100	300 × 320	940	Φ8@80	0.42	1.26	3.75
A-5 (5)	C50	40	180 × 200	540	Φ8@135	0.42	3.35	10.01
A-6 (6)	C50	60	220 × 240	340	Φ8@135	0.34	2.29	6.82
A-7 (7)	C50	80	260 × 280	940	Φ8@125	0.26	1.66	4.95
A-8 (8)	C50	100	300 × 320	740	Φ6@105	0.18	1.26	3.75
A-9 (9)	C40	40	180 × 200	740	Φ6@125	0.26	3.35	10.01
A-10 (10)	C40	60	220 × 240	940	Φ6@145	0.18	2.29	6.82
A-11 (11)	C40	80	260 × 280	340	Φ8@95	0.42	1.66	4.95
A-12 (12)	C40	100	300 × 320	540	Φ8@100	0.34	1.26	3.75
A-13 (13)	C30	40	180 × 200	940	Φ6@95	0.34	3.35	10.01
A-14 (14)	C30	60	220 × 240	740	Φ8@110	0.42	2.29	6.82
A-15 (15)	C30	80	260 × 280	340	Φ6@125	0.18	1.66	4.95
A-16 (16)	C30	100	300 × 320	540	Φ8@130	0.26	1.26	3.75

Note: The thickness of the protective layer of the test piece related to the longitudinal ribs is 25 *mm*; the configuration of the longitudinal ribs of the test piece is 6Φ16 (HRB335); the number in the parentheses of the test piece is the number corresponding to the picture (photo) at the back.

dial gauge) are collected and monitored by the computer at the right time.

Measurement of internal bond-slip is as follows: The relative slip (distribution) of the profiled flange and web on the concrete joint is measured directly by the slip sensor prepositioned inside and outside and web surfaces of the profiled flange and the measured data are collected and monitored by the computer at the right time. The test loading and testing device are shown in Figure 11.

4.3. Test Results and Analysis

4.3.1. Failure Mode and Process of the Test Piece. The final failure mode of a part of the test piece in the axial pull-out test of steel-reinforced concrete is shown in Figure 12.

(1) Bonding Splitting Failure. This kind of damage occurs in specimens with low reinforcement ratio, thin thickness of profile steel protective layer, and long embedded part of profile steel. In the test, most of the axes pulled out of the test piece suffered such damage. Destruction characteristics are as follows: the test piece has a short duration from initial

cracking to failure. When the fracture occurs, the crack penetrates the entire specimen along the longitudinal direction of the profile steel. At the initial stage of loading, there are basically no cracks in the test piece, and there is no relative slip between the profile steel and concrete. When the load reaches the ultimate bond load of 20% to 40%, the chemical bond force in the bond force at the loading end of the test piece is basically lost. There is a slight slip between profile steel and concrete (about 0.05 mm), but there is still no crack on the surface of the concrete; as the load increases, the slip at the loading end gradually increases; when the load reaches about the ultimate bond load of 80%, vertical splitting cracks begin to appear on the inner side of the steel wing margin protection layer loaded at the end of the specimen (the parts where cracks appear vary slightly with the thickness of the protective layer). Then, as the load increases, the crack gradually extends outward in the direction of about 45° or parallel to the profile steel flange and gradually extends to the length of the profile steel; after the load reaches the ultimate bond load (i.e., the test piece reaches the ultimate bond strength), the crack passes through the upper and lower parts of the test piece and extends to the full length. The hooping begins to bend and
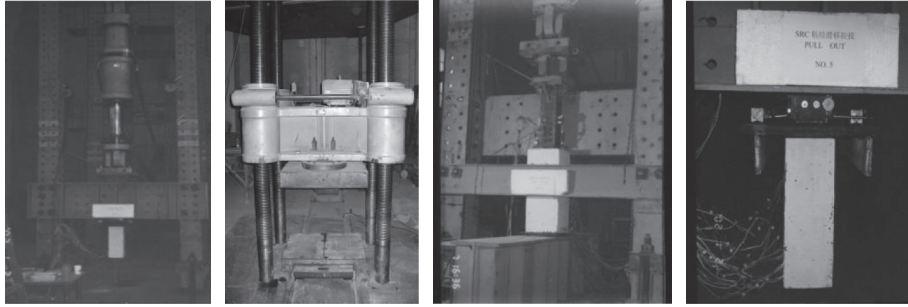
FIGURE 11: Test loading and testing device.
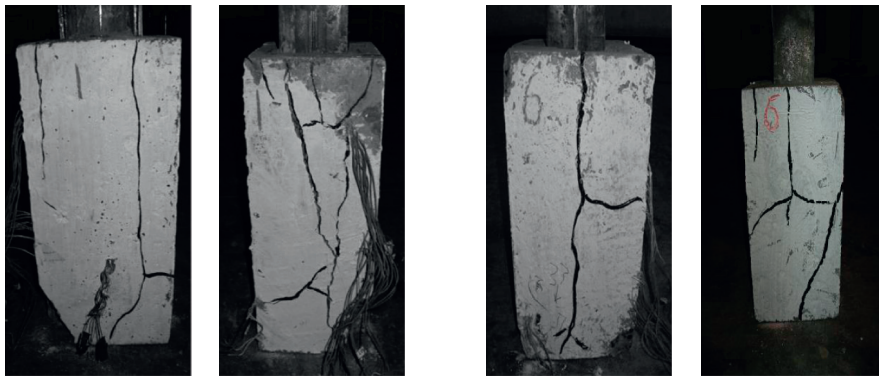
A-1: C60, c =40 mm,
l_0 =340 mm, ρ_{sv} =0.18%

A-6: C50, c =60 mm,
l_0 =340 mm, ρ_{sv} =0.34%
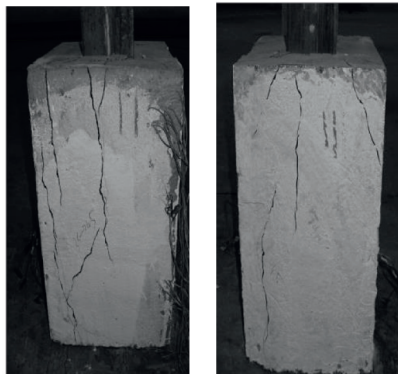
A-11: C40, c =80 mm,
l_0 =340 mm, ρ_{sv} =0.42%

A-15: C30, c =60 mm,
l_0 =340 mm, ρ_{sv} =0.18%
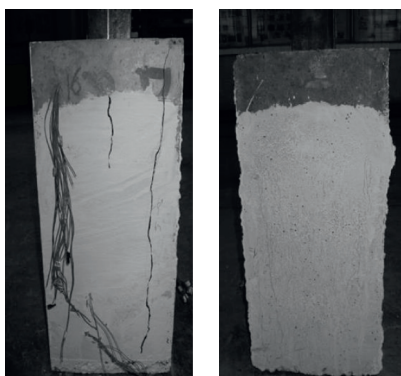
A-12: C40, c =100 mm,
l_0 =540 mm, ρ_{sv} =0.34%
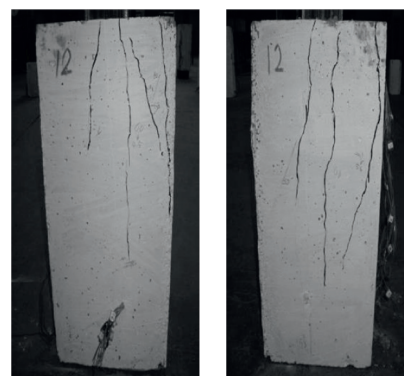
A-16: C30, c =100 mm,
l_0 =340 mm, ρ_{sv} =0.26%

FIGURE 12: Pulling out the final crack and damage state of the test piece.

the profile steel is slowly pulled out, but is not bent yet. Longitudinal shear occurs between profile steel and concrete. However, due to the different design parameters of the test pieces, the crack width and failure process are clearly different, and the thickness of the protected layer and the anchor length have a significant impact. When the anchoring length is larger (>720 mm) and the thickness of the protective layer is relatively smaller (≤ 60 mm), the crack is smaller, and the damage process is relatively slow. When the anchorage length is smaller (≤720 mm) and the thickness of the protective layer is larger (>60 mm), the crack is larger, and the damage process is relatively sudden. When the loading end slip is larger, the influence of the hoop ratio on the damage begins to be obvious: the number and width of the cracks of the test piece with a large hoop ratio (≥ 0.30%) hardly increase; and the crack width of the specimen with a lower hoop ratio (<0.30%) continues to increase until they are connected.

The bonding splitting failure belongs to brittle failure and should be avoided in the design of steel-reinforced concrete structural components.

(2) Bond Anchorage (i.e., Steel Pull-Out) Failure. This damage occurs in the test piece with a relatively large hoop ratio, shorter profile steel buried, and a large thickness of the profile steel protective layer. In the test, the damage occurred in specimens A-11 and A-15 pulled out of the axis. Destruction characteristics are as follows: when the load reaches about 80% of the ultimate bond load, the microcracks perpendicular to the flange begin to appear on the inner side of the steel wing margin protection layer loaded at the end of the test piece but then continue to load until the profile steel is pulled out. The shear cracks on the inside of the protective layer around the profile steel are mainly extended to the full length of the profile steel within a small thickness range and expanded slightly to the outside of the protective layer. The hooping and the profile steel are usually in an elastic working state. After the test, it was found that the surface of the extracted profile steel was accompanied by a layer of crushed concrete powder and was mixed with fine particles.

The bond anchorage failure is also a brittle failure and should be avoided in the design of steel-reinforced concrete structural components.

(3) Profile Steel (under Tension) Yield Failure. This damage occurs in the test piece with a large hoop ratio, thick steel protective layer, and long profile steel buried. In the test, the A-4 specimen pulled out of the axis caused such damage destruction characteristics: before the load reaches the tensile yield load (i.e., the tensile profile steel yield reaches the tensile yield strength), the test piece has almost no cracks, and there is no obvious relative slip between the profile steel and concrete; when the load is close to the tensile yield load (i.e., the profile steel is close to the tensile yield strength), the crack occurs locally at the loading end of the test piece, and the crack width and the relative slip amount of the profile steel are small. After that, if the loading continues, the profile steel (end) is

usually subjected to tensile yield and undergoes strengthening during the stage until it is pulled out.

The profile steel (under tension) yield failure is ductile failure; that is, the bond bearing capacity (or bond strength) between profile steel and concrete is greater than the tensile ultimate bearing capacity (or tensile strength) of profile steel. In the design of steel-reinforced concrete structural components, it (under tension) should be advocated.

4.3.2. The Comparison of Test Results and Theoretical Calculation Results. There are many factors involved in the bond-slip of steel-reinforced concrete, which are concealed and difficult to measure. Therefore, in previous research and engineering practice on bond-slip of steel-reinforced concrete, it is often used to simplify the problem by using the value of the applied load at the loading end of the test piece and the relative slip between the profile steel and concrete measured. Then the average bonding stress along the anchorage length of the profile steel is derived, and the relationship between the average bonding stress and the relative slip of the profile steel and concrete at the loading end of the test piece is fitted. In this way, the data are obtained from the test about the load value of the loading end of various test pieces and the relative slip between profile steel and concrete is statistically analyzed, and the simplified calculation formulas of average bonding stress and average bond strength which are convenient for engineering practice are proposed. The relationship between the average bonding stress along the (full) anchorage length and the effective anchorage length of the profile steel and the relative slip between the loaded-end steel and the concrete of the specimen are given, respectively. This research will lay a theoretical foundation for the study of the conversion rules of the steel-reinforced concrete bond-slip along the anchoring length of the profile steel.

In the numerical calculation, it is assumed that the spring damage index $D(\varepsilon)$ and the friction block damage index $D_f(\varepsilon)$ follow the same evolution law [6]:

$$D(S) = 1 - \exp\left[-\frac{1}{2}\left(\frac{S - S_0}{aS_0}\right)^2\right] \quad S \geq S_0, \qquad (13)$$

$$D_f(S) = 1 - \exp\left[-\frac{1}{2}\left(\frac{S - S_0}{bS_0}\right)^2\right] \quad S \geq S_0, \qquad (14)$$

where a and b are parameters related to the component size.

Equations (13) and (14) are substituted into equations (11) and (12). The *P-S* mean value curve and single variance fluctuation curve of the steel-reinforced concrete can be calculated. The corresponding test curves of A-13 and A-14 are shown in Figure 13.

Figure 13 shows the mean *P-S* curve calculated by the spring-friction block model theory and the fluctuation range of the *P-S* curve with one-fold variance as the changing amplitude. It can be seen that the variation law of the *P-S* test curve of each test piece is consistent with the change rule of the *P-S* curve of mean value being calculated theoretically. Among them, the *P-S* test curves of test pieces A-10 and
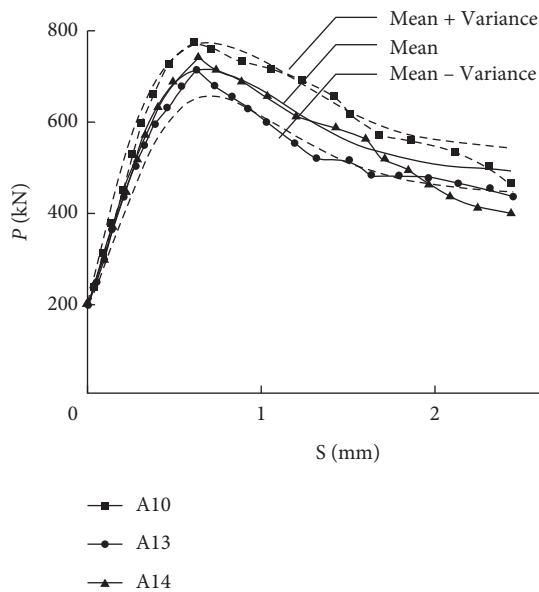
FIGURE 13: Comparison of numerical calculation of *P-S* curve and test curve.

A-14 all fall within the range of one-fold variation of the mean value, and most of the test curves of test piece A-13 also fall within the range of one-fold variation of the mean value. It is shown that the theoretical model of spring-friction block stochastic damage established in this paper can simulate the *P-S* transformation law of the interface between profile steel and concrete in the mean sense, and it can accurately predict the error range brought by the constitutive relationship analysis results due to the discreteness of concrete material properties and the randomness of defects.

5. Summary of This Chapter

This paper presents a model of the bond-slip stochastic failure of the interface. Through theoretical analysis and experimental verification, the following conclusions are drawn:

(1) Based on the research on the bonding effect of steel-reinforced concrete, the mechanism of bond-slip failure at the interface of steel-reinforced concrete was analyzed.

(2) According to the distribution of chemical bonding force, frictional resistance, and mechanical bite force at the interface between profile steel and concrete and the transformation law between them, a mesoscopic model based on spring-friction block is established.

(3) Considering the discreteness of concrete performance and the randomness of defects and applying the stochastic damage theory, according to the energy transformation and conservation law of damage evolution process, the stochastic failure model of steel-reinforced concrete surface is established.

(4) The comparison between the numerical results of the model and the tensile test results of reinforced concrete shows that the theoretical model of stochastic destruction of spring-friction blocks can well average the simulate value of the *P-S* conversion rule at the interface of the profile steel and concrete, and the model can accurately predict the error range brought about by the constitutive relationship analysis results due to the dispersion of the properties of the concrete material performance and the randomness of the defects. This model will provide a theoretical basis for the simulation analysis of the refined damage of steel-reinforced concrete structures [15].

Data Availability

All the data, models, and code generated or used during the study appear in the submitted article.

Conflicts of Interest

The authors declare that they have no conflicts of interest.

Acknowledgments

References

[1] M. F. Bado, J. R. Casas, and G. Kaklauskas, "Distributed Sensing (DOFS) in Reinforced Concrete members for reinforcement strain monitoring, crack detection and bond-slip calculation," *Engineering Structures*, vol. 226, Article ID 111385, 2021.

[2] R. Z. Al-Rousan and A. M. Abu-Elhija, "Predicting the bond-slip relationship between concrete and CFRP using anchoring holes technique," *Case Studies in Construction Materials*, vol. 13, Article ID e00462, 2020.

[3] M. Zhu, T. Ueda, and J.-H. Zhu, "Generalized evaluation of bond behavior of the externally bonded FRP reinforcement to concrete," *Journal of Composites for Construction*, vol. 24, p. 6, 2020.

[4] Y. Pang, G. Wu, H. Wang, D. Gao, and P. Zhang, "Bond-slip model of the CFRP-steel interface with the CFRP delamination failure," *Composite Structures*, vol. 256, Article ID 113015, 2021.

[5] A. Yazarlu and M. Dehestani, "Application of discrete element method (DEM) in characterization of bond-slip behavior in RC beams with confinement subjected to corrosion," *Structure*, vol. 28, pp. 1965–1976, 2020.

[6] S.-B. Kang, S. Wang, X. Long, D.-D. Wang, and C.-Y. Wang, "Investigation of dynamic bond-slip behaviour of reinforcing bars in concrete," *Construction and Building Materials*, vol. 262, Article ID 120824, 2020.

[7] M. Li, Z. Liu, Z. Yang, Z. Wang, and H. Yuan, "Bond-slip behaviors between reinforced concrete and coated rebar via a new strain monitoring method and FEA simulation," *Construction and Building Materials*, vol. 262, Article ID 120402, 2020.

[8] F. Yu, T. Chen, K. Niu, S. Wang, Z. Kong, and Y. Fang, "Study on bond-slip behaviors of self-stressing steel slag concrete-filled steel tube," *KSCE Journal of Civil Engineering*, vol. 24, no. 11, pp. 3309–3319, 2020, Prepublish.

[9] S. Zheng, G. Deng, Y. Yang, M. Yu, and J. Zhang, "Experimental study on bond-slip performance between steel shape and concrete in SRC structures," *Engineering Mechanics*, vol. 20, no. 5, pp. 63–69, 2003.

[10] C. W. Roeder, R. Chmielowski, and C. B. Brown, "Shear connector requirements for embedded steel sections," *Journal of Structural Engineering*, vol. 125, no. 2, pp. 142–151, 1999.

[11] G. Deng, *Experimental Research and Basic Theoretical Analysis of Bond Slip Performance of Steel Reinforced concrete Structures*, Doctoral thesis, Xian University of Architecture and Technology, Xi'an, China, 2004.

[12] A. Esin and W. J. D. Jones, "A theory of fatigue based on the microstructural accumulation of strain energy," *Nuclear Engineering and Design*, vol. 4, no. 3, pp. 292–298, 1966.

[13] W.-Z. Yang and J. Li, "A stochastic damage constitutive relation for concrete material subjected to biaxial tensile loading," *Chinese Quarterly of Mechanics*, vol. 32, no. 4, pp. 590–596, 2011.

[14] J. Eibl and B. Schmidt-Hurtienne, "STRAIN-RATE-SENSITIVE constitutive law for concrete," *Journal of Engineering Mechanics*, vol. 125, no. 12, pp. 1411–1420, 1999.

[15] S. Zheng, G. Deng, and Y. Yang, "Experimental study on bond slip performance of section steel concrete structure," *Engineering Mechanics*, vol. 20, no. 5, pp. 64–69, 2003.

Research Article

Seismic Resistance Properties of Improved Dry-Type Beam-Column Joint: An Experimental Research

Wei Ma,[1,2,3] **Fan Yang,**[2] **Pan Hu,**[2] **Haiyi Liang** [ID],[1] **and Kai Xu**[2]

[1]*University of Science and Technology of China, Hefei 230601, China*
[2]*Anhui Jianzhu University, Hefei 230601, China*
[3]*Architectural Design and Research Institute of Anhui Jianzhu University, Hefei 230601, China*

Correspondence should be addressed to Haiyi Liang; hyliang@ustc.edu.cn

Dry-type joints are an advanced type of sustainable beam-column connection mode used in the prefabricated concrete frame structural system. This paper proposed an improvement scheme for high-strength bolt dry-type joints and designed a new type of common bolt dry-type joints. A pseudo test involving low-cycle repeated loading is conducted to assess the seismic resistance properties of new joints including damage mode, hysteretic curve, skeleton curve, and ductility factor. Numerical simulation is applied to validate the rationality of experimental results. It is found that when the bending capacity of the end block of the beam is consistent with that of the bolt, the deformation of the bolt will no longer increase greatly after a period of large deformation; at this period, the bolt does not fully enter the plastic stage, but at this time, the end block of the beam begins to appear large cracks and enter the plastic deformation and has good energy dissipation performance.

1. Introduction

Prefabrication is considered as the best way to realize building industrialization and sustainable construction because of its socio-economic and environmental advantages such as higher construction efficiency, better controlled quality, and less waste and pollution compared with the traditional cast-in-place method [1, 2]. Joints, as the most vulnerable part of the whole prefabricated structural system, usually determine the capacity of whole structure [3, 4]. The failure of joints sometimes results in the failure of the whole building. Therefore, the design of joints is the key link in prefabricated structure design. The construction of cast-in-place joints requires a lot of wet work on-site, which will produce more waste and pollution.

Currently, the most common types of beam-column joints for prefabricated concrete frame structures are cast-in-place joints and welded joints. The construction of cast-in-place joints requires a lot of wet work on-site, which will generate much waste and pollution. Because of the need for high temperature, welded joints need to consume a large

amount of energy and emit carbon dioxide. Both of them are not sustainable enough [5–11]. Dry-type joints are the latest development. All structural components fastenings are all prefabricated in factories, and connection between beam and column members is realized by bolt on-site. These advanced joints can not only reduce negative environmental impacts caused by construction activities but also have good mechanical properties and structural performance [12, 13].

Our project group has designed a new dry-type joint using high-strength bolts to achieve good antiseismic behavior [14, 15]. Experimental results show that this new dry-type joint can have good ductility and energy dissipation capacity. However, the design still has many disadvantages. First and foremost, the displacement of high-strength bolts is very small in the process of experiment. This means they cannot dissipate energy efficiently. In addition, the size of reserved holes is not big enough, which caused that reserved holes are likely to be blocked when grouting in the gap.

Based on identified disadvantages of previous design, this paper aims to (1) improve the design of dry-type joint; (2) test the seismic resistance properties of improved joint

through a pseudo-static experiment approach; and (3) validate the feasibility and mechanism of the proposed improved design scheme through numerical simulation. Research results can not only enrich the structural systems of prefabricated buildings but also contribute to the knowledge body of sustainable construction in general.

2. Materials and Methods

2.1. Specimen Design. In order to better understand and compare the seismic resistance properties of the improved dry-type joints, the new test specimen is the same in size as the specimen before the improvement. The beams and columns in the test specimen are both prefabricated components, in which the strength grade of longitudinal bars and stirrups is both HRB400. The pressure plates and bolts are made of Q345 steel. The column is made of concrete with strength grade C80 and section size of 750×750 mm. Eight bolt holes with the diameter of 40 mm are reserved in symmetrical position on the upper part of the bracket on the column. The beam is made of concrete with strength grade C40. The section size of the "T" expanded end of the beam is 750×750 mm, and the section size of the beam body is 400×750 mm. Eight bolt holes with the diameter of 50 mm are reserved for the "T" expanded end of the beam. After the beam and column are placed in the corresponding position, they are connected and fixed with a steel long bolt with a diameter of 28 mm through reserved holes. The 20 mm gap at the junction the "T" expanded end of the beam and column was filled by sleeve grout, and a 40 KN pretightening force was applied to each bolt by electric torque wrench. The three-dimensional diagram of the new improved common bolt dry-type beam-column joint is shown in Figure 1, and the size and reinforcement of specimen are shown in Figure 2.

It is necessary to point that we have tested high-strength bolt in previous experiment, where some shortcomings had been found; thus, a new beam was assembled by a new kind of joint, which had no difference with previous joint except bolt strength. To address the shortcomings existing in the previous high-strength bolt dry-type beam-column joints, the following improvements were made in terms of test specimen design and installation:

(1) High-strength bolts are replaced with common bolts, and the bolt size is reduced from 30 mm to 28 mm.

(2) The reserved bolt holes at "T" expanded end of the beam are expanded from 40 mm to 50 mm. This makes the installation process more convenient without the need for later adjustment and repair.

(3) The reserved holes were perforated by PC tubes so that the mortar in the gap is not likely to flow into the holes. This can help to prevent reserved holes from bee blocked when grouting.

The material property test was conducted before the experiment according to the standard of the mechanical properties test method of ordinary concrete (GB/T50152-2012) [16]. The measured compressive strength of concrete is shown in Table 1. The measured diameter, yield strength, ultimate strength, and elongation of steel bars and bolts are shown in Table 2.

Figure 3 displays the stress position of bolt, which provides support for predicting the strength of bolt.

$$M_0 = \left(F_1 L_1 + F_2 L_2 + F_3 L_3 \right) \times 2. \tag{1}$$

From geometric relations,

$$F_3 = \frac{1}{3} F_1,$$
$$F_2 = \frac{2}{3} F_1, \tag{2}$$

$$F_1 = f_y S = 374 \times 3.14 \times \left(\frac{28}{2} \right)^2 = 230.17 KN, \tag{3}$$

where f_y refers to the yield strength of bolt and S refers to the cross sectional area of bolt.

According to (2), $F_2 = 153.45$ KN and $F_3 = 76.72$ KN.
According to (1), $M_0 = 388$ KN•$m = 0.85 \times 456$ KN•m.
The design is reasonable.

2.2. Test Loading Device and Loading System. This experiment was completed in the Key Laboratory of Structure and Underground Engineering of Anhui Jianzhu University. The test loading equipment was the 500 KN electro-hydraulic servo loading system with the displacement stroke of the actuator produced by Beijing Foli Company. The test loading device is shown in Figure 4.

A pseudo-static test of low-cycle repeated loading is adopted in this experiment [17, 18]. The free end of the beam is subjected to a low-cycle repeated load by the actuator. The force-displacement controlled combined loading system (Figure 5) is applied. The full loading process is divided into two stages. Initially, the force controlled loading is used before the specimen yields. Each grade was loaded 5 KN and cycled once. Then, displacement controlled loading was used when the specimen yields. Each grade was 20 mm and cycled three times until the specimen failed. At the same time, a constant axial pressure of 1080 KN was applied to the column top by hydraulic jack during the test, and the corresponding design axial pressure ratio was 0.05.

2.3. Arrangement and Selection of Test Points. In order to collect relevant test data, the strain of concrete and reinforcement was measured on the precast members, respectively. The main location of the strain is shown in Figure 6 where LS represents the bolt strain, Z represents the reinforcement strain on column, L represents the reinforcement strain on beam, and H represents the concrete strain. Two displacement sensors were installed at the bottom of the beam to measure the displacement deformation of the precast beam under low cyclic reciprocating load, which are shown in Figure 7.
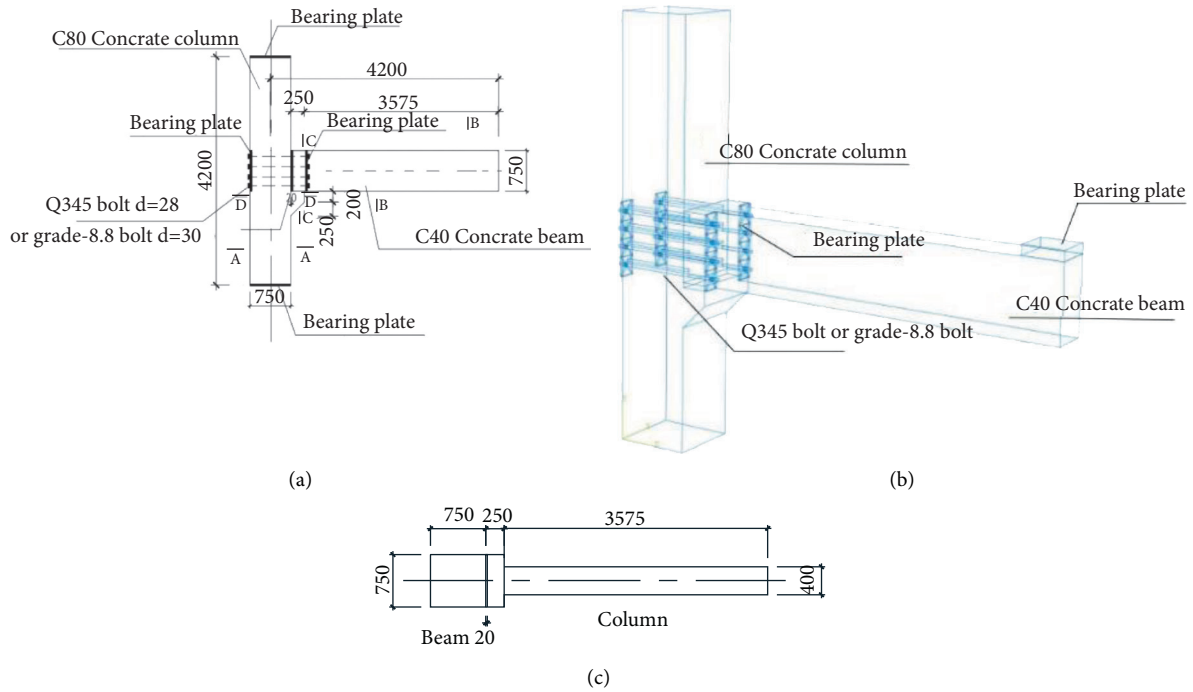
Figure 1: Specimen design drawing: (a) elevation plan; (b) a three-dimensional joint diagram; (c) top view.
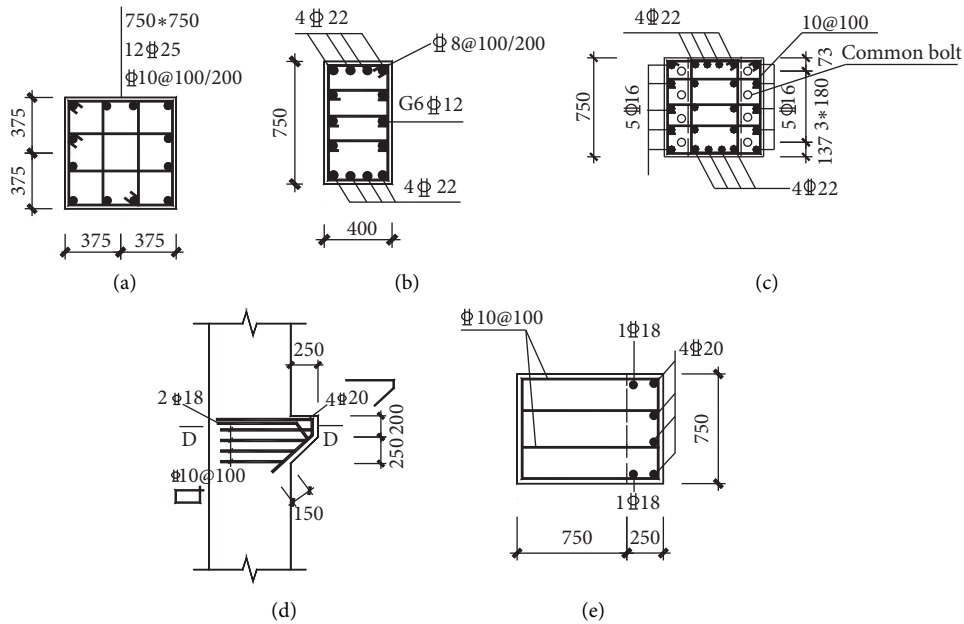
Figure 2: Reinforcement drawing of specimen: (a) A-A sectional drawing; (b) B-B sectional drawing; (c) C-C sectional drawing.

Table 1: Performance parameters of concrete (unit: N/mm).

Concrete strength	3 days	7 days	28 days
C40	26.53	38.31	50.31
C40	27.28	37.52	47.52
C40	26.45	38.63	49.34
C80	27.30	77.30	84.36
C80	28.20	78.22	87.12
C80	27.90	77.91	85.46

TABLE 2: Performance parameters of steel bars and bolts (unit: N/mm²).

Type	Rebar/bolt diameter d (mm)	Yield strength, f_{yk}	Ultimate strength, f_{stk}	Elongation
HRB400	12	465.2	577.3	21.6%
HRB400	14	447.4	567.6	23.2%
HRB400	16	437.6	620.4	23.2%
HRB400	18	456.4	589.6	22.6%
HRB400	22	421.3	571.9	19.6%
HRB400	25	456.6	605.7	20.2%
Q345 bolt	28	380.2	516.8	17.9%
Grade-8.8 bolt	30	618.7	785.2	11.4%
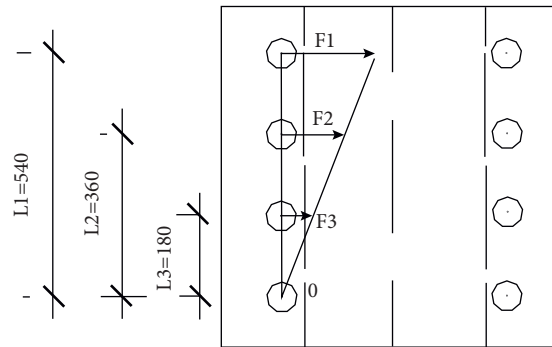
FIGURE 3: Stress position of bolt.

(a)   (b)
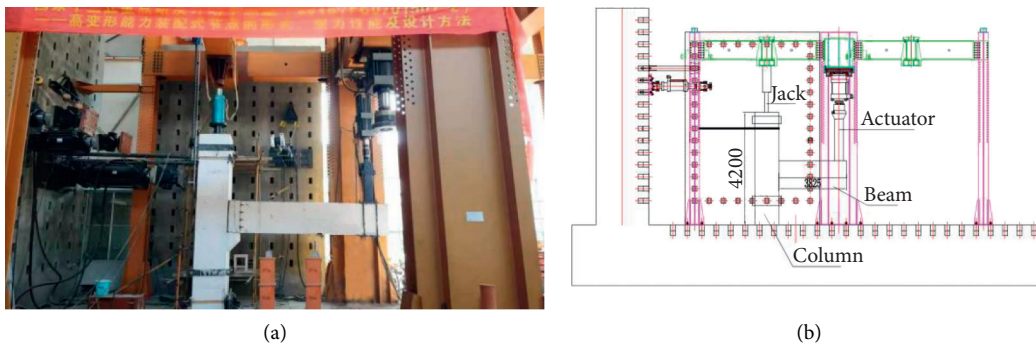
FIGURE 4: Loading diagram: (a) field photo; (b) design diagram.
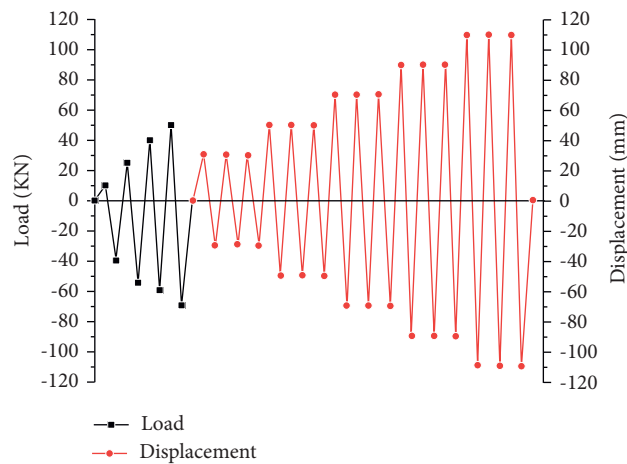
FIGURE 5: Load regime diagram.
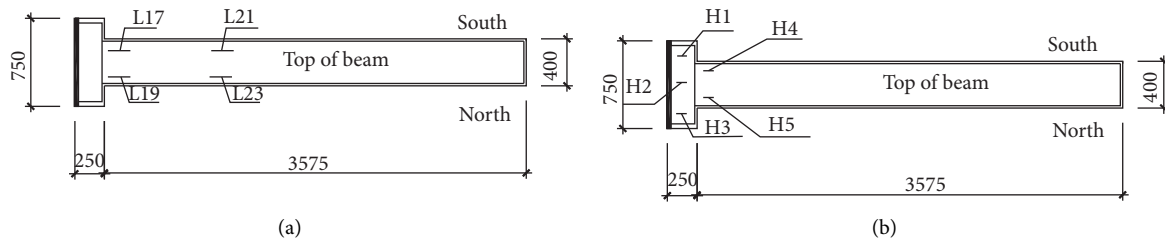
FIGURE 6: Location map of main strain gauge: (a) beam top steel strain gauge position; (b) position of concrete strain gauge on top of beam.

FIGURE 7: External displacement meter layout.

3. Results and Discussion

3.1. Experimental Phenomenon. The test loading direction stipulates that pushing down refers to positive direction (+), pulling up refers to the negative direction (−), and the loading order is positive before negative. At the initial stage of the force controlled loading, the deformation and strain of the specimen did not change significantly, and no cracks occurred. When loaded to +25 KN, the first crac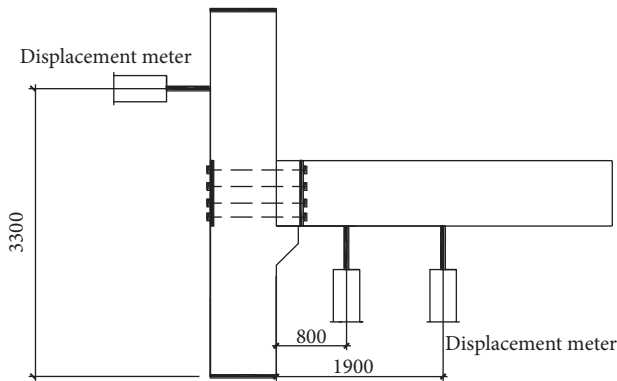k of 0.06 mm width occurred at the junction of beam "T" expanded end and beam body, and a crack of 0.09 mm appeared on the grouted gap surface. When reversely loaded to −55 KN, symmetric cracks occur on the bottom surface and the upper surface of the beam. With the increase in the loaded force, the beam continues to crack and the crack width develops. The strain of the longitudinal reinforcement and the bolt of the beam increases gradually. When loaded to −80 KN, a large displacement deformation was observed on the beam. The crack width at the grouted gaps increased to 2.76 mm, and the reinforcement strain at the "T" expanded end of the beam changed suddenly. This indicates that longitudinal reinforcement yields.

Then, displacement controlled loading was applied to replace force controlled loading. When the loaded to +30 mm, the crack width at the grouted gaps reached 3.84 mm. When loaded to +70 mm, a crack appeared at the top with a width of 0.2 mm and a crack width of 5.3 mm, and the crack width at the grouted gaps reached 5.3 mm. When loaded to −90 mm, there were deep penetrating cracks formed at the bottom of the beam and the crack width at the grouted gaps reached 10 mm. When loaded to +110 mm, the concrete at the "T" expanded end of the beam is partially crushed and the test specimen failed.

The final failure mode and crack trend of the beam are shown in Figures 8 and 9.

By comparing the test phenomena of different specimens, we can see that the load borne by the first crack in P1 (assembled by common bolt) is less than that of the first crack in P2 (assembled by high-strength bolt). The common bolts in P1 deform during the whole loading process while the high-strength bolts in P2 do not deform and the stress value does not reach the yield strength. The generation and development trend of the cracks in the two specimens gradually developed from the t-shaped end of the precast beam to the end of the beam with the continuous increase in the load. Besides, the width of the crack kept increasing as well. At last, both of them were damaged due to crushing of the concrete at the t-shaped end of the precast beam.

3.2. Comparative Analysis. In this section, the improvement of seismic resistance properties of normal bolt dry-type joint (P1) is evaluated by comparing the failure characteristics, hysteretic curve, skeleton curve, and ductility coefficient with the figure for previous high-strength bolt dry-type joint (P2) tested under the same experimental conditions. It is necessary to note that the only difference between the two specimens is the type of the bolt; others including reinforcement, strength of concrete, and size of beam are all the same.

3.2.1. Failure Characteristics. P1 and P2 have many similarities in failure characteristics. There were no cracks appearing on the column or the bracket during the whole test process. The initial cracks firstly appeared at the "T" expanded end of the beam. With the increase in load, the number of cracks gradually increased and the cracks developed from the "T" expanded end to the tail of the beam body. The concrete at the "T" expanded end of the beam is finally crushed, and the whole specimen failed. However, the failure of P1 is more ductile than that of P2. In addition, the common bolt in P1 has a large deformation, while the high-strength bolt in P2 has no significant deformation.

3.2.2. Hysteretic Curve. The hysteretic curves of the two specimens are shown in Figure 10. It can be seen from the figure that the variation trends of hysteretic curve of the two specimens are similar. In the initial stage of loading, the load and displacement of the two specimens both show a linear relationship, indicating that both are in the elastic stage.

Common Bolt

(a)

Grade-8.8 Bolt

(b)

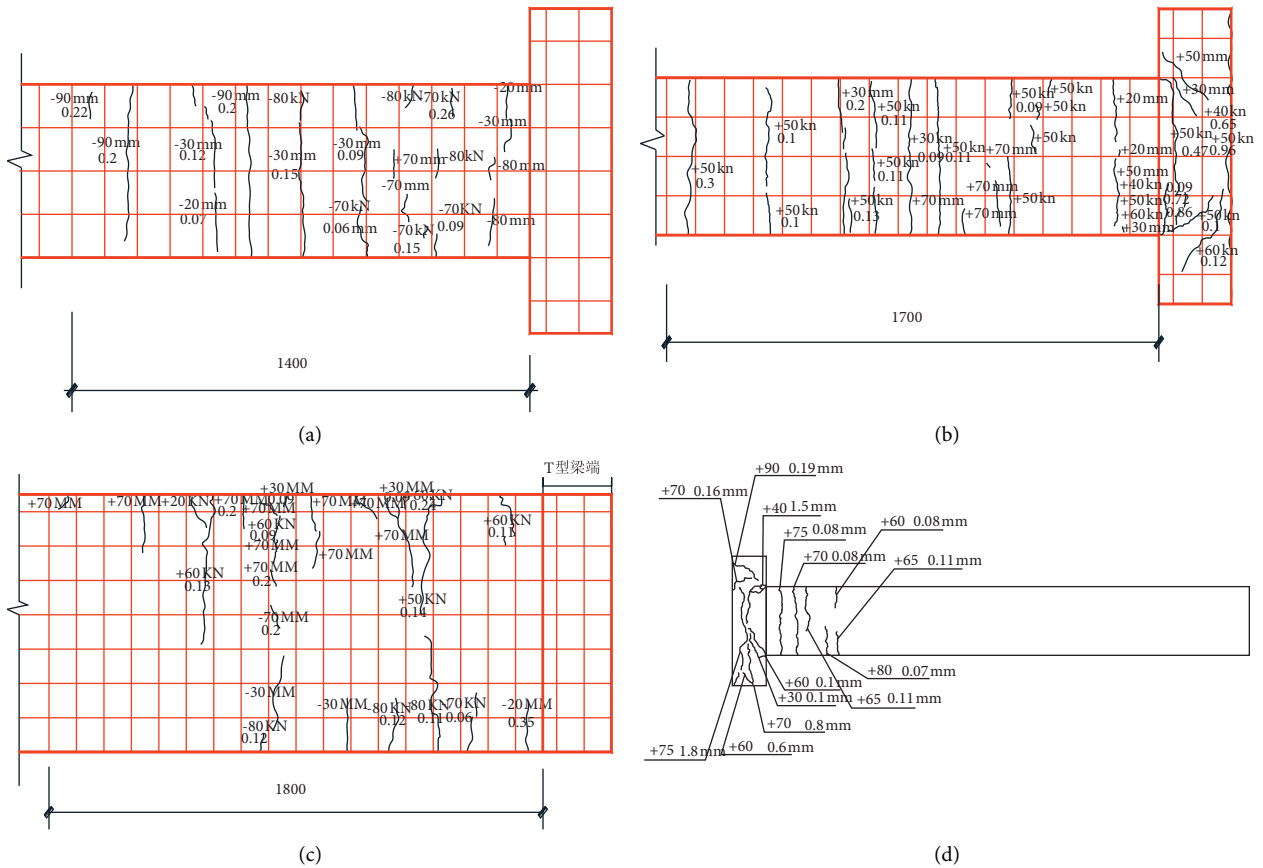FIGURE 8: Specimen failure local diagram: (a) common bolt; (b) Grade-8.8 bolt.

(a)

(b)
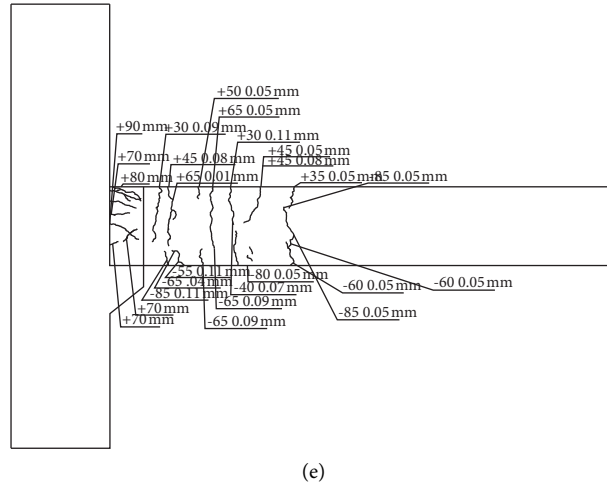

(c)

(d)

FIGURE 9: Continued.

(e)

FIGURE 9: Crack diagram of specimen. (a) Distribution diagram of crack diagram on bottom of beam. (b) Distribution diagram of crack diagram on top of beam. (c) Distribution diagram of crack diagram on side of beam. (d) Distribution diagram of cracks on top of beam. (e) Distribution diagram of cracks on side of beam.
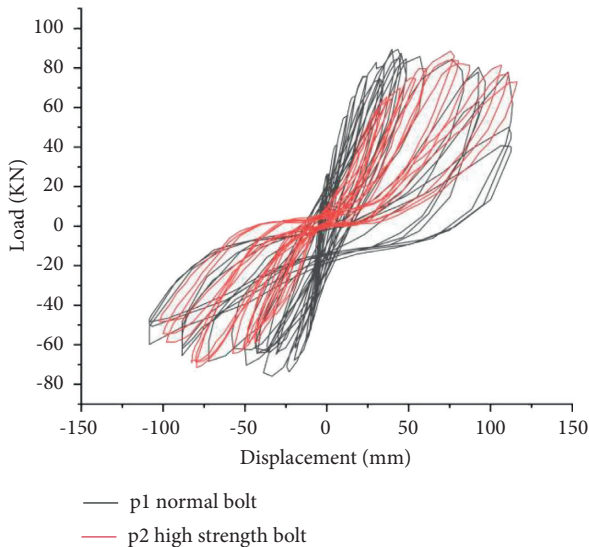

FIGURE 10: Load-displacement control hysteresis curve.

With the increase in load, the longitudinal reinforcement at the "T" expanded end of the beam yields. The slope of hysteretic curve gradually increases and the area of the hysteretic ring also increases, indicating that the plastic deformation of the two specimens gradually increases, and both specimens have good energy dissipation capacity.

However, the comparison shows that the hysteresis ring of P1 is plumper than that of P2, indicating that P1 has stronger energy dissipation capacity and better seismic resistance properties. The displacement of P1 is obviously larger than that of P2 in the elastic phase, indicating that P1 has better deformation capacity. The "pinching" effect of specimen P2 is more obvious than that of P1, indicating that there is a serious slip of reinforcement in P2.

3.2.3. Skeleton Curves. The skeleton curves of the two specimens are shown in Figure 11. It can be learned that the skeleton curves of the two specimens have similar change trends with obvious descending segments, indicating that both the two specimens have good ductility. However, the descending section of P1 is more gentle compared with that of P2. This indicates that P1 has better ductility.

3.2.4. Ductility Coefficients. The ductility coefficients of the two specimens are shown in Table 3. Compared with P2, the ductility coefficient of P1 increased from 2.17 to 3.05 with an improvement of 40.5%, which proved that the ductility of P1 performance was better once again.

4. Numerical Simulation

4.1. Transformation between Parameters of Concrete Plastic Damage Model. For the concrete plastic damage model provided in ABAQUS, the stress-strain curve of compression and tension beyond the elastic part shall be in the form of $\sigma_c - \tilde{\varepsilon}_c^{in}$, and $\sigma_t - \tilde{\varepsilon}_t^{in}$ must be input with positive value; otherwise, the operation will be interrupted automatically with an error. The stress-strain curve of compression and tension for the concrete plastic damage model is shown in Figure 12. And the calculation formula is as follows:

Compression stage:

$$\begin{cases} \tilde{\varepsilon}_c^{in} = \varepsilon_c - \varepsilon_{oc}^{el}, \\ \varepsilon_{oc}^{el} = \dfrac{\sigma_c}{E_0}. \end{cases} \tag{4}$$
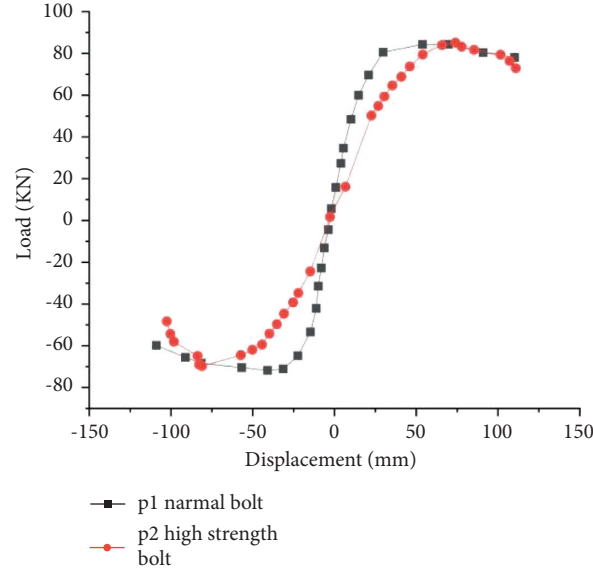
FIGURE 11: Load-displacement control skeleton curve.

TABLE 3: Analysis table of ductility factor (unit: mm).

Type	Direction of action	Yield displacement	Limit displacement	Ductility factor	
P1	Pull	24.48	78.47	3.21	3.05
	Press	29.07	83.68	2.88	
P2	Pull	48.20	95.30	1.97	2.17
	Press	46.90	110.90	2.36	
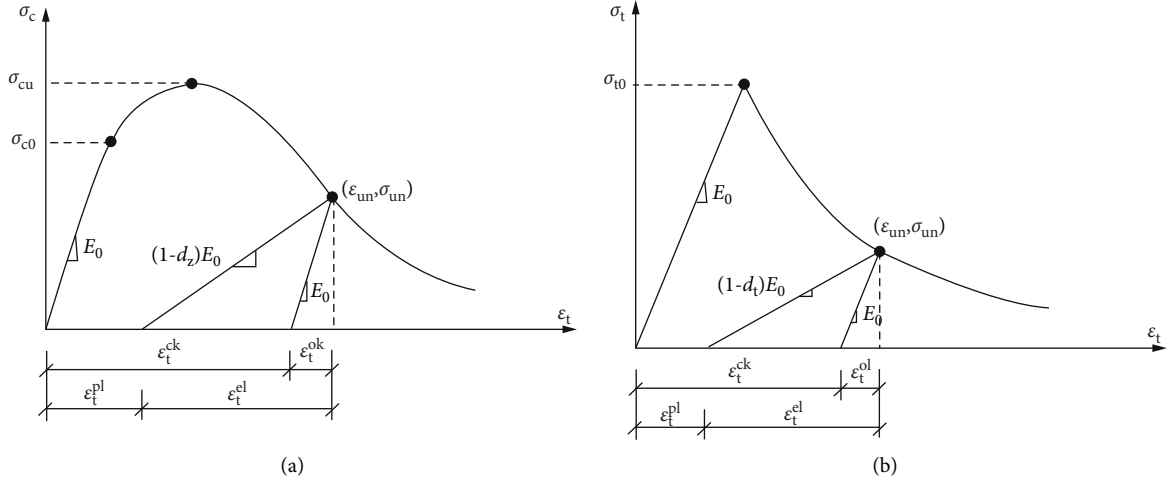
FIGURE 12: Curve of the concrete damage plasticity model: (a) compression stage; (b) tensile stage.

Tensile stage:

$$\begin{cases} \widetilde{\varepsilon}_t^{ck} = \varepsilon_t - \varepsilon_{0t}^{el}, \\ \widetilde{\varepsilon}_{0t}^{el} = \dfrac{\sigma_t}{E_0}. \end{cases} \quad (5)$$

When the compression and tension damage data are input into ABAQUS, the inelastic strain will be automatically converted into plastic strain through the following formula. If the plastic strain is less than 0, ABAQUS will report an error and cannot conduct operation.

$$\text{Compression stage: } \widetilde{\varepsilon}_c^{pl} = \widetilde{\varepsilon}_c^{in} - \frac{d_c}{(1-d_c)} \cdot \frac{\sigma_c}{E_0}, \quad (6)$$

$$\text{Tensile stage: } \widetilde{\varepsilon}_t^{pl} = \widetilde{\varepsilon}_t^{ck} - \frac{d_t}{(1-d_t)} \cdot \frac{\sigma_t}{E_0}. \quad (7)$$

In equations (6) and (7), E_0 is the initial elastic modulus of concrete; $\widetilde{\varepsilon}_c^{pl}$ and $\widetilde{\varepsilon}_c^{in}$ are compression plastic strain and

<div align="center">(a)</div>

<div align="center">(b)</div>
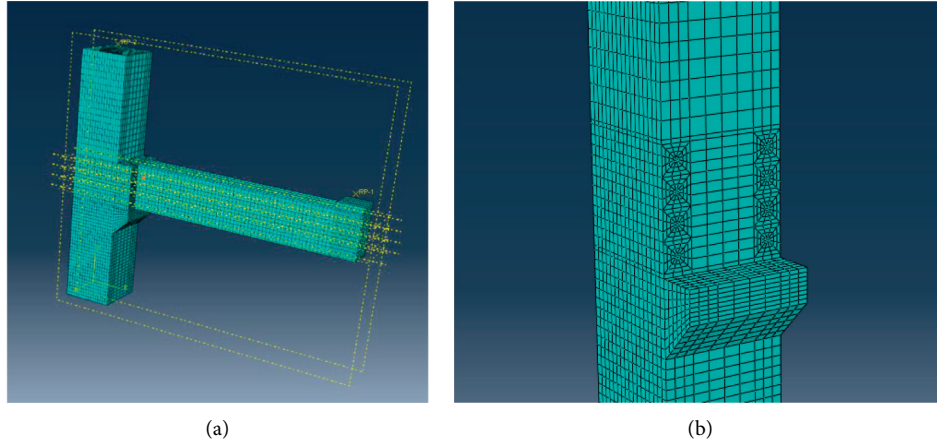
FIGURE 13: Finite element model: (a) grid plot of specimen; (b) local grid.

compression inelastic strain of concrete, respectively; $\widetilde{\varepsilon}_t^{pl}$ and $\widetilde{\varepsilon}_t^{ck}$ are tensile plastic strain and tensile inelastic strain of concrete, respectively; $\widetilde{\varepsilon}_{0c}^{el}$ and $\widetilde{\varepsilon}_c^{el}$ are, respectively, the compressive elastic strain when concrete is not damaged and the compressive elastic strain considering damage; and $\widetilde{\varepsilon}_{0t}^{el}$ and $\widetilde{\varepsilon}_t^{el}$, respectively, are the tensile elastic strain when the concrete is not damaged and the elastic strain considering the damage;

4.2. Finite Element Modelling. Finite element analysis software ABAQUS [19–22] is used to simulate the seismic resistance properties of the new dry-type joints assembled by the common bolt in this paper. The reinforcement adopts the three-dimensional two-node T3D2 element, and its properties are set with the double-fold model; concrete adopts three-dimensional solid reduction integral C3D8R element, and its properties are set with the concrete plastic damage model. Embedded technology is applied to realize the coupling between concrete and reinforcements. The established finite element model is shown in Figure 13(a). Due to the existence of bolt holes, the mesh quality has a great influence on the model convergence during numerical simulation. Therefore, it is necessary to carry out fine mesh cutting and division of bolt holes. The mesh of irregular parts around bolt holes is shown in Figure 13(b).

4.3. Failure Mode. Figure 14 shows the equivalent plastic strain cloud diagram, which is used in numerical simulation to represent the plastic damage degree of concrete, of the specimen with common bolt dry-type joint. And Figure 15 shows the failure of precast beam in experiment. It can be seen from the simulation results that except the severe damage to the "T" expanded end end of the beam, there is basically no damage to other parts. In the real test, the ultimate failure model of the specimen was concrete in the middle part of the "T" expanded end of the beam crushing, while other parts were basically intact. Therefore, the simulation results are consistent with the test results, indicating that the test results are not accidental.

4.4. Analysis of Bolt Deformation. The bolt stress-strain cloud diagrams of the two specimens are shown in Figure 16. It can be found that during the whole test process, the high-strength bolt was not damaged and there was even no obvious deformation leading to a limited unloading capacity. The main reason was that the high-strength bolt had high yield strength. The plastic failure of concrete occurs prior to bolt yield failure. After the improvement, the maximum strain of common bolt increases by about 120% compared with high-strength bolt. The energy can be dissipated through the deformation of bolt, thus improving the dynamic property of the dry-type joint and the capacity of the whole structure. At the same time, using common bolts instead of high-strength bolts can also help to save engineering costs.

In addition, the numerical simulation results show that the common bolt does not yield completely. Therefore, the capacity of structure can be further improved by increasing the ratio of reinforcement at the "T" expanded end of the beam.

4.5. Comparative Analysis of Hysteresis Curve. The comparison of hysteresis curves between simulation and test, both of which were assembled with common bolt, is shown in Figure 17. These results show the two have good energy dissipation capacity and seismic performance. Because of ignoring the sliding effect of reinforcement in the finite element simulation, the finite element simulation result is plumper than the experiment. At the beginning of the test loading, the two are in the linear state, which indicates that the test is in the elastic stage. With the increase in the loading displacement, the hysteresis loop area also increases. It indicates that the test enters the nonlinear stage. During the loading process, the setting of boundary conditions cannot reach the ideal fixed state and then the loading of the force may cause slight looseness to the boundary constraints of the specimen. As a result of it, the positive and negative hysteretic curves obtained by the test are not completely symmetric. Therefore, the simulation results are in good agreement with the experimental results.
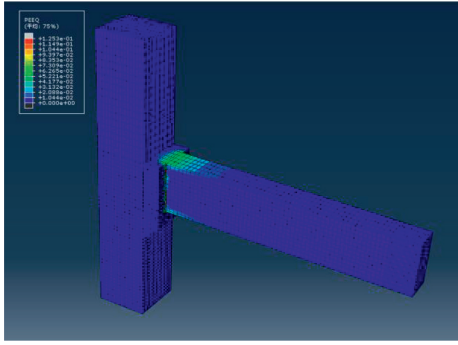
Figure 14: Equivalent plastic strain nephogram of concrete.
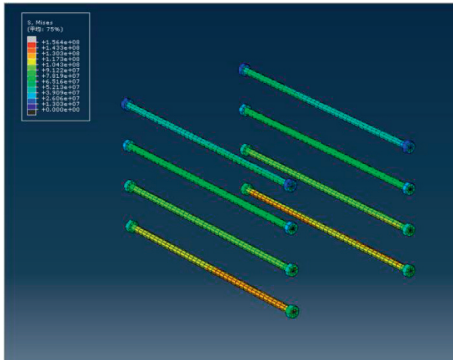

Figure 15: Failure diagram of precast beam.

Figure 16: Stress-strain nephogram of bolt.

Figure 17: Comparison between numerical simulation and experiment skeleton curves.

5. Conclusions and Recommendations

5.1. Conclusions. The previous high-strength bolt dry joint has some shortcomings. This paper puts forward an improvement scheme and designs a new common bolt dry-type joint in order to solve this problem. A series of pseudo-static tests are carried out to assess the improvement of seismic resistance properties of new joints. The failure mode, hysteretic curve, skeleton curve, and ductility coefficient of the two specimens with high-strength bolt and common bolt are compared. The rationality of the test results is verified by numerical simulation. The main conclusions are as follows:

(1) Compared with high-strength bolt dry-type joints, the hysteretic curve of the improved common bolt dry-type joints is plumper, the descending section of the skeleton curve is more stable, and the ductility coefficient is higher. This means improved common bolt dry-type joints have better seismic resistance properties.

(2) The improved common bolt dry-type joint is more convenient to install. The bolt hole is not easily blocked. It is more environmental and cost-effective. Therefore, new joints have good practicability.

(3) Compared with high-strength bolts, common bolts can generate larger deformation, which makes the linked beam and column components have better rotation ability. Therefore, common bolts can improve the ductility and capacity of the whole prefabricated concrete frame structure.

The improved common bolt dry-type joint has better seismic resistance properties and practicability, which proves the feasibility of the improved scheme. The results of this paper can be applied to enrich the prefabricated structural systems and the knowledge of sustainable construction. In addition, the new dry joint proposed in this paper can be applied to various prefabricated concrete frame structures due to its good economic and environmental benefits.

5.2. Recommendations.

(1) During the test, the bolt still did not reach the yield strength although the common bolt had a large deformation compared with the high-strength bolt. Finally, the concrete of the beam was crushed before the bolt was damaged. This failure mode is not expected. In the later research, the seismic resistance properties of the joints can be further improved by optimizing the reinforcement ratio of the "T" expanded end of the beam.

(2) In this paper, finite element software ABAQUS is used to effectively simulate the seismic resistance properties of the new dry-type joints. More attention can be paid to how to apply numerical simulation to further optimize the design of this advanced joint, thus saving the time and economic cost brought by experimental research.

Data Availability

The data used to support the findings of this study are available from the corresponding author upon request.

Conflicts of Interest

The authors declare that there are no conflicts of interest regarding the publication of this paper.

Acknowledgments

References

[1] Y. F. Wang and Z. J. Yang, "On the development of prefabricated building," *Chinese & Overseas Architecture*, vol. 2017, no. 1, pp. 57–59, 2017, in Chinese.

[2] X. K. Huang and C. Y. Tian, "Research on prefabricated concrete structure," *Housing Industry*, vol. 2010, no. 9, pp. 27–32, 2010.

[3] M. N. S. Hadi and T. M. Tran, "Seismic rehabilitation of reinforced concrete beam–column joints by bonding with concrete covers and wrapping with FRP composites," *Materials and Structures*, vol. 49, no. 1-2, pp. 467–485, 2016.

[4] N. Shajil, S. M. Srinivasan, and M. Santhanam, "An experimental study on self-centering and ductility of pseudo-elastic shape memory alloy (PESMA) fiber reinforced beam and beam-column joint specimens," *Materials and Structures*, vol. 49, no. 3, pp. 783–793, 2015.

[5] G. W. Yang, C. J. Che, S. N. Xiao, B. Yang, T. Zhu, and S. Jiang, "Experimental study and life prediction of bolt loosening life under variable amplitude vibration," *Shock and Vibration*, vol. 2019, Article ID 2036509, 8 pages, 2019.

[6] C. X. Wu, Y. F. Zhang, C. Zhang, X. S. Deng, and Y. Zhou, "Study on seismic behavior of precast concrete beam column joints," *Earthquake resistant engineering and Retrofitting*, vol. 37, no. 1, pp. 83–90, 2015.

[7] X. L. Gao, L. B. Xu, J. Li, and Y. Cao, "Experimental analysis on mechanical behavior of precast concrete beam column joints," *Journal of Huazhong University of Science and Technology(Natural Science Edition)*, vol. 44, no. 10, pp. 47–52, 2016.

[8] J. H. Zhao, Y. Hu, D. F. Zhang, and C. Chen, "Experimental study on seismic behavior of prefabricated composite CFST column steel beam frame," *Journal of Building Structures*, vol. 41, no. 8, pp. 88–96, 2020.

[9] D. Chen, L. Ding, and C. Y. Shao, "Finite element simulation of FRP connectors for prefabricated sandwich panel," *Journal of Anhui Jianzhu University*, vol. 25, no. 6, pp. 8–14, 2017.

[10] W. Ma, Y. Li, and K. W. Ding, "Mechanical properties of new dry-type beam-column bolt connection joint," *Sustainability*, vol. 11, pp. 1–14, 2019.

[11] Y. Li, *Comparative Study on Mechanical Properties of New Fabricated concrete Beam-Column Dry Joints*, Anhui Jianzhu University, Hefei, China, 2020.

[12] Y. Chen, Q. Gao, and Z. Q. Guan, "Self-loosening failure analysis of bolt joints under vibration considering the tightening process," *Shock and Vibration*, vol. 2017, Article ID 2038421, 15 pages, 2017.

[13] X. W. Li, "Load transfer characteristics of a cable bolt in DEPT," *Shock and Vibration*, vol. 2019, Article ID 2106741, 10 pages, 2019.

[14] China Architecture & Building Press, *Code For design of concrete structures (GB50010-2010)*, China Architecture & Building Press, Beijing, China, 2011.

[15] China Architecture & Building Press, *Technical Specification for Precast concrete Structures(JGJ 1-2014)*, China Architecture & Building Press, Beijing, China, 2014.

[16] China Architecture & Building Press, *Standard for Test Methods of concrete structures(GB/T50152-2012)*, China Architecture & Building Press, Beijing, China, 1978.

[17] China Architecture & Building Press, *Code Of Seismic Test For Buildings (JGJ/T101-2015)*, China Architecture & Building Press, Beijing, China, 2015.

[18] C. Fang, Y. Ping, and Y. Chen, "Loading protocols for experimental seismic qualification of members in conventional and emerging steel frames," *Earthquake Engineering & Structural Dynamics*, vol. 49, no. 2, pp. 155–174, 2019.

[19] Y. Z. Wang and C. G. Fu, *Examples And Detailed Explanation of Structural Engineering Analysis of ABAQUS*, China Architecture & Building Press, Beijing, China, 2010.

[20] Z. Zhuang, X. C. You, and J. H. Liao, *Finite Element Analysis and Application Based on ABAQUS*, Tsinghua university press, Beijing, China, 2009.

[21] Y. Q. Long, *Introduction of Finite Element Method*, People's Education Press, Beijing, China, 1978.

[22] L. S. Chu, G. J. Li, D. D. Li, and J. Zhao, "Study on progressive collapse behavior of SRC column-steel beam hybrid frame based on pushdown analysis," *Shock and Vibration*, vol. 2017, Article ID 3075786, 12 pages, 2017.

Research Article

Insights into Underrail Rubber Pad's Effect on Vehicle-Track-Viaduct System Dynamics

Linya Liu,[1] **Zhiyuan Zuo,**[1] **Yunlai Zhou** [ID],[2] **Jialiang Qin,**[1] **and Zhenyu Niu**[1]

[1]*Engineering Research Center of Railway Environment Vibration and Noise, Ministry of Education, East China Jiaotong University, Nanchang 330013, China*
[2]*State Key Laboratory for Strength and Vibration of Mechanical Structures, School of Aerospace Engineering, Xi'an Jiaotong University, Xi'an 710049, China*

Correspondence should be addressed to Yunlai Zhou; yunlai.zhou@xjtu.edu.cn

To scientifically characterize the dynamic mechanical characteristics of the rubber pad under the rail of fasteners and its influence on the dynamic response of the vehicle-rail-viaduct system, taking the rubber pad under the rail of WJ-7B high-speed railway (HSR) with constant resistance as an example, a TFDV model was applied to characterize the viscoelasticity of the rubber pad and the theoretical model in the dynamic coupling of vehicle-rail-bridge was also studied. The results show that the energy storage modulus and loss factor of rubber pad under rail show a curved surface relation versus the change of frequency-temperature. In a certain frequency/temperature range, the energy storage modulus and loss factor of rubber pad under rail increase with the decrease of temperature and the increase of frequency, and the influence of low temperature on dynamic parameters is more significant. With the decrease of temperature, the minimum value of total dynamic flexibility decreases, and the corresponding extreme frequency shifts to high frequency. Viscoelastic dynamic features of rubber pad under rail mainly affect the dynamic response of vehicle subsystem and rail-bridge subsystem. With the decrease of ambient temperature of rubber pad, the dominant frequency band of power spectrum curve of each structure shifts to high frequency.

1. Introduction

High speed railway (HSR) serves as the effective solution to reduce the private transport and enhance the public transport, as well to reorganize the urban zone due to its high load, fast speed, high safety, and comfort. HSR has developed rapidly in China [1–3]. Because the elevated bridge track transportation can occupy less land and can more reliably control the long-term settlement of the foundation, it has good line smoothness and stability [4, 5]. When a high-speed train is running on a bridge, the wheel-rail system will vibrate severely due to the irregularity and be transmitted to the foundation under the rail, which will cause the vibration of the vehicle-track-bridge system, leading to the change of the operating quality and service life [6]. To ensure the high quality of high-speed rail operation, high-speed rail tracks often use rail fasteners

with higher flexibility. The fastener not only is a necessary connecting device in the railway structure, but also plays a role of track vibration reduction. The main component that provides vibration reduction performance is the under-rail rubber pad in the fastener. In previous studies on vibration of vehicle-track-bridge systems at home and abroad, the dynamic mechanical parameters (stiffness, damping) of under rail rubber pads often adopt fixed values [7–10]. Because the underrail rubber pad component contains rubber polymer materials, its mechanical performance parameters under dynamic force are not constant. According to the literature [11–15], rubber polymer materials have viscoelasticity (referring to the mechanical properties of rubber materials under the influence of factors such as ambient temperature and excitation frequency which are also called temperature/frequency dynamic characteristics). This dynamic

mechanical characteristic will change the dynamic mechanical parameters of the underrail rubber pad [16], which will affect the vibration response of the vehicle-track-viaduct system.

Relevant research studies were carried out on the dynamic parameters of rail fasteners. Yin et al. [17] analyzed the effect of the frequency variation characteristics of fastener's stiffness on wheel-rail vibration and noise based on the vehicle-track coupling dynamics theory and acoustic theory; Wang et al. [18, 19] used mathematical method and virtual excitation method to analyze the vehicle-rail vertical coupled random vibration considering the frequency change of the fastener pad's stiffness. The effect of the viscoelastic dynamic characteristics of the rubber pad on the vertical coupled vibration of the vehicle-rail-viaduct system is still rarely studied.

To explore the influence of viscoelasticity of the rubber pad under the track on the vehicle-track-viaduct vertical coupling dynamic response and accurately predict the dynamic response of the vehicle-track-viaduct system, this study takes the underrail rubber pad of the HSR WJ-7B constant resistance fastener as example and establishes a constitutive model that comprehensively considering the viscoelasticity of the under-rail rubber pad, and uses genetic algorithm to identify the structural model parameters by combining the established constitutive model with the separated parameter model and the vehicle-rail-viaduct coupled vibration frequency domain model to form a frequency domain viaduct vibration model that takes into account the viscoelastic dynamic characteristics of the underrail rubber pad. The viscoelasticity effect of underrail rubber pads on the dynamic response of the vehicle-rail-viaduct system is studied.

2. Vehicle-Rail-Viaduct Coupling Model

Dynamic flexibility method is used to construct the vehicle-rail-bridge coupling model shown in Figure 1. Since the parameters involved in the calculation of vehicle-track coupled vibration in the under-rail pad are stiffness and loss factor, it is necessary to convert the modulus value into a stiffness value according to the structural size of the material. The calculation is as follows:

$$k_f = \frac{AE_s}{h}, \tag{1}$$

where k_f indicates the stiffness of the rubber pad under the rail and A and h mean the bottom effective area (according to the actual bearing area and the measured size of the rubber pad under the rail, the effective area is reduced by 30% of the actual size) and thickness of the rubber pad under the buckle rail, respectively. E_s is the storage modulus of the rubber pad under the rail.

The vehicle-rail-viaduct coupling dynamics model used in this study is shown in Figure 2. The vehicle system uses the CRH380A high-speed train, using a 10-DOF longitudinal half-vehicle model of a single carriage [20]. The rail is simplified to be an infinite length Timoshenko beam; the track plate and the base version are simplified to

Euler–Bernoulli beams with free ends, and the bridge is simplified to a simple supported Euler beam at both ends. Fasteners, CA mortar layer, sliding layer, and bridge support are all considered as discrete viscoelastic support unit [21]. The model calculation process is shown in Figure 3.

2.1. Vehicle Vibration Model.

The vertical vibration equation of a single carriage is as follows:

$$[M_v]\{\ddot{Z}_v\} + [C_v]\{\dot{Z}_v\} + [K_v]\{Z_v\} = \{P_v\}, \tag{2}$$

where $[M_v]$ means the quality matrix of the carriage; $[C_v]$ represents the damping matrix of the carriage; $[K_v]$ indicates the stiffness matrix of the carriage; $\{Z_v\}$, $\{\dot{Z}_v\}$, and $\{\ddot{Z}_v\}$ indicate the displacement, velocity, and acceleration of the carriage, respectively, and $\{P_v\}$ denotes the wheel-rail force.

Separating the variables of (2) shall obtain

$$[\beta_w] = \frac{[Z_w]}{\{P_v\}}, \tag{3}$$

where $[\beta_\omega]$ means the dynamic flexibility matrix of the wheel at the wheel-rail contacting point and $[Z_\omega]$ represents the vertical displacement matrix of the wheel pair.

2.2. Track-Viaduct Vertical Coupled Vibration Model.

The rail viaduct coupling system mainly includes steel rails, track plate, base plate, and box beams. Fasteners connect the rail and track plate, and CA mortar connects the track plate and base plate, and sliding layers connect the base plates and box beams. The box type beams are supported by bearings installed on the piers.

The rail is simplified as Timoshenko beam, and its dynamic flexibility is as follows [22]:

$$\beta(x_1, x_2) = u_1 e^{-ik_1|x_1-x_2|} + u_2 e^{-ik_2|x_1-x_2|}. \tag{4}$$

The vibration displacement of the rail is as follows:

$$Z_r(x) = \sum_{w=1}^{N_w} \beta_r(x, x_w)P_w - \sum_{n=1}^{N} \beta_r(x, x_n)F_{fn}, \tag{5}$$

where P_w means the wheel-rail force of wth wheel pair; N_w means the amount of the wheel pair; F_{fn} means the nth fastener's force; and N means the amount of the fasteners for certain rail with 32 m.

The base plate and bearing plate are simplified as free-free Euler–Bernoulli beam, and the dynamic flexibility is as follows:

$$\beta_b(x_1, x_2) = \sum_{n=1}^{N} \frac{\varphi_n(x_1)\varphi_n(x_2)}{\left[\omega_n^2(1+i\eta) - \omega^2\right]}, \tag{6}$$

where $\varphi_n(x)$ means the nth order mode shape at the x location, ω_n represents the nth resonant circular frequency of free-free Euler beam, ω denotes the excitation circular frequency, η indicates the loss factor, and N describes the cutting-off order.
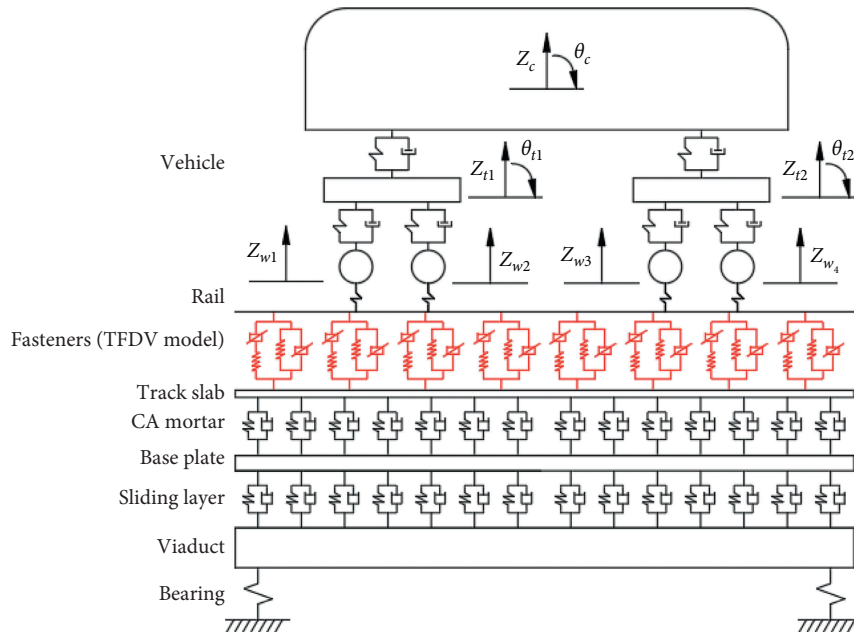
The displacement of the track plate follows:

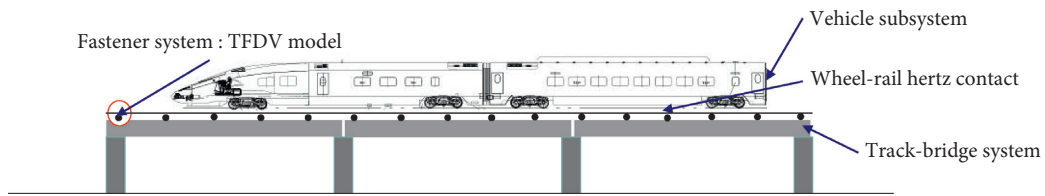Figure 1: Vertical coupling vibration analysis of vehicle-rail-bridge.

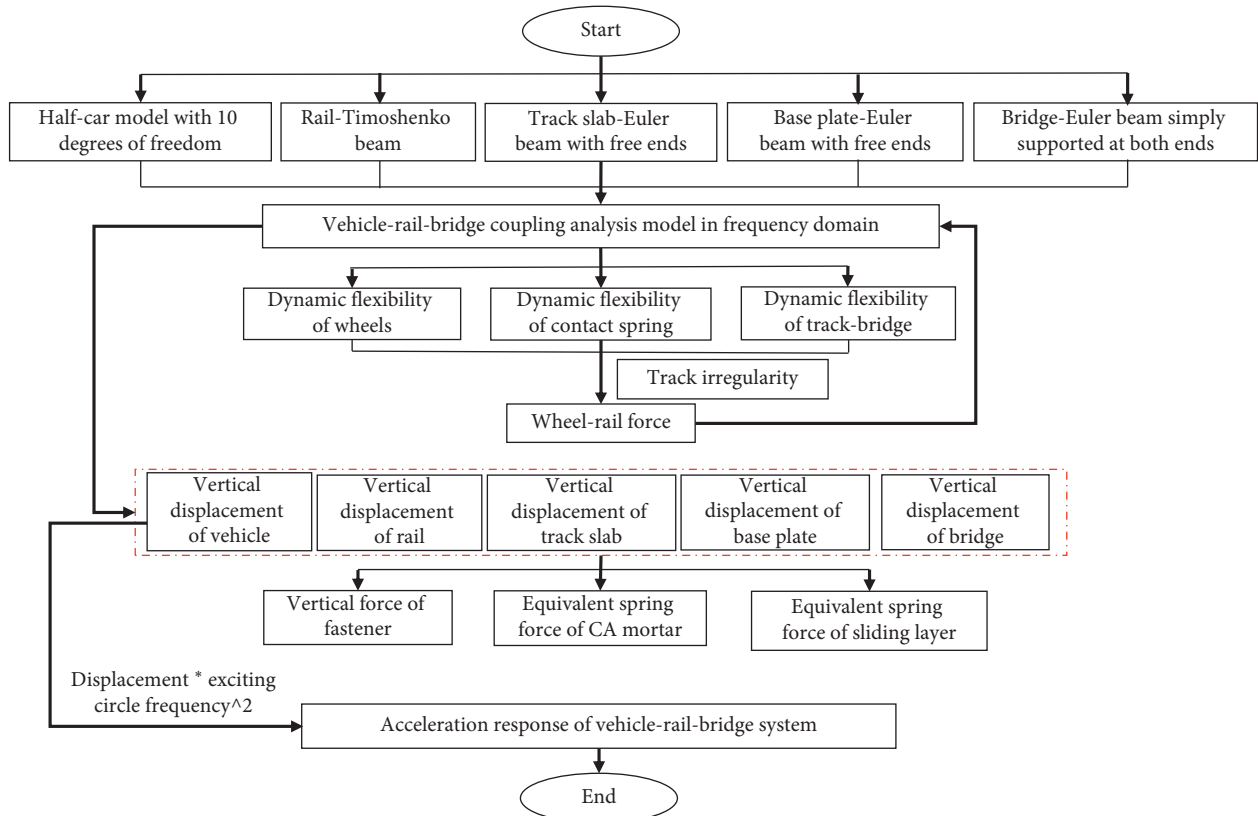Figure 2: Subsystems of the vehicle-rail-viaduct system.

Figure 3: Calculation flow chart.

$$Z_s(x) = \sum_{n=1}^{N} \beta_s(x, x_n) F_{fn} - \sum_{m=1}^{M} \beta_s(x, x_m) F_{jm}, \qquad (7)$$

where F_{fn} means the nth fastener's force, N means the amount of the fasteners, F_{jm} means the nth discrete spring force at CA mortar layer, and M means the amount of the discrete springs.

When calculating the dynamic flexibility of the base plate, the base plate is simplified as a free-free Euler–Bernoulli beam, and its dynamic flexibility is as follows:

$$\beta_d(x_1, x_2) = \sum_{n=1}^{N} \frac{\varphi_n(x_1)\varphi_n(x_2)}{\left[\omega_n^2(1 + i\eta) - \omega^2\right]}, \qquad (8)$$

where $\varphi_n(x)$ means the nth mode shape at the xth location, ω_n indicates the nth order circular frequency, ω means the circular frequency, η means the loss factor, and N means the cutting-off order.

The displacement of the base plate is

$$Z_d(x) = \sum_{m=1}^{M} \beta_d(x, x_m) F_{jm} - \sum_{h=1}^{H} \beta_d(x, x_h) F_{zh}, \qquad (9)$$

where F_{jm} is the discrete spring force of the mth CA mortar layer, F_{zh} is the discrete spring force of the hth sliding layer, M is the amount of discrete springs in the CA mortar layer, and H is the amount of discrete springs in the sliding layer.

The viaduct is simplified as simply supported Euler beam, and the dynamic flexibility is expressed as

$$\beta_d(x_1, x_2) = \sum_{n=1}^{N} \frac{\varphi_{bn}(x_1)\varphi_{bn}(x_2)}{\left[\omega_{bn}^2(1 + i\eta_b) - \omega^2\right]}, \qquad (10)$$

where $\varphi_{bn}(x)$ means the nth order mode shape of the simply supported beam, ω_{bn} means the nth order resonant frequency, N means the amount of the modes, and ω means the excitation circular frequency.

The displacement of the viaduct is as follows:

$$Z_b(x) = \sum_{h=1}^{H} \beta_b(x, x_h) F_{zh} - \sum_{i=1}^{2} \beta_b(x, x_{qi}) F_{qi}, \qquad (11)$$

where F_{qi} means the force applied by the ith bearing to X_{qi} on the viaduct.

The fastener force F_{fn}, mortar layer discrete support force F_{jm}, sliding layer discrete support force F_{zh}, and bearing force F_{qi} are as follows:

$$\begin{cases} F_{fn} = K_f\left(Z_r(x_n) - Z_s(x_n)\right), \\ F_{jm} = K_j\left(Z_s(x_m) - Z_d(x_m)\right), \\ F_{zh} = K_z\left(Z_d(x_h) - Z_b(x_h)\right), \\ F_{qi} = K_q Z_b(x_i), \end{cases} \qquad (12)$$

where K_f means complex stiffness for fasteners; K_j means discrete spring complex stiffness for CA mortar layer; K_z means sliding layer discrete spring complex stiffness; and K_q means discrete spring complex stiffness for bridge support. And certain complex stiffness factors are as follows:

$$\begin{cases} K_f = k_f\left(1 + i\eta_f\right), \\ K_j = k_j\left(1 + i\eta_j\right), \\ K_z = k_z\left(1 + i\eta_z\right), \\ K_q = k_q\left(1 + i\eta_q\right), \end{cases} \qquad (13)$$

where k_f η_f mean the stiffness and the loss factor of the fastener, respectively; k_j, η_j represent the stiffness and loss factor of the CA mortar layer, respectively; k_z, η_z indicate the stiffness and loss factor of the sliding layer, respectively; and k_q, η_q denote the stiffness and loss factor of the viaduct bearing, respectively.

Substituting (14) into (5), (7), (9) and (11) can obtain

$$\begin{cases} Z_r(x) + \sum_{n=1}^{N} \beta_r(x, x_n) K_f Z_r(x_n) - \sum_{n=1}^{N} \beta_r(x, x_n) K_f Z_s(x_n) = \sum_{w=1}^{N_w} \beta_r(x, x_w) P_w \\[2mm] -\sum_{n=1}^{N} \beta_s(x, x_n) K_f Z_r(x_n) + Z_s(x) + \sum_{n=1}^{N} \beta_s(x, x_n) K_f Z_s(x_n) + \sum_{m=1}^{M} \beta_s(x, x_m) K_j Z_s(x_m) - \sum_{m=1}^{M} \beta_s(x, x_m) K_j Z_d(x_m) = 0 \\[2mm] -\sum_{m=1}^{M} \beta_d(x, x_m) K_j Z_s(x_m) + Z_d(x) + \sum_{m=1}^{M} \beta_d(x, x_n) K_j Z_d(x_m) + \sum_{h=1}^{H} \beta_d(x, x_h) K_z Z_d(x_h) - \sum_{h=1}^{H} \beta_d(x, x_h) K_z Z_b(x_h) = 0 \\[2mm] -\sum_{h=1}^{H} \beta_b(x, x_h) K_z Z_s(x_h) + Z_b(x) + \sum_{h=1}^{H} \beta_b(x, x_h) K_z Z_b(x_h) + \sum_{i=1}^{I} \beta_B(x, x_i) K_q Z_b(x_i) = 0. \end{cases}$$

$$(14)$$

Equation (14) can be written in matrix form:

$$[\beta K]\{Z\} = \{P\}, \qquad (15)$$

where $[\beta K]$ means result of the dynamic flexibility multiplied with complex stiffness of each structural layer of the rail viaduct system; $\{Z\}$ means the displacement matrix of

each layer of rail viaduct system; and $\{P\}$ means the load matrix.

From (15), the dynamic flexibility of the rail viaduct coupling system follows

$$\beta^{TB} = \frac{Z^{TB}}{P}, \tag{16}$$

where Z^{TB} means displacement of rail viaduct coupling system under wheel-rail force and β^{TB} denotes dynamic flexibility representing the displacement of the rail viaduct coupling system under unit harmonic force.

2.3. Wheel-Rail Contact Model.
Assuming the wheel-rail contact as Hertz contact, k_c means the contact spring stiffness coefficient; the dynamic flexibility follows

$$\beta^c = \frac{1}{k_c}. \tag{17}$$

2.4. Virtual Excitation Method.
This section computes the vehicle-rail-viaduct random dynamic responses via the virtual excitation method. Assuming the first wheel-rail contact point to be uneven, the power spectrum density (PSD) is $S_{rr}(\omega)$, and the virtual excitation vector of the two wheel pairs of the entire carriage follows

$$\mathbf{R}(\omega) = \left\{ 1 e^{-2i\omega l_t/V} e^{-2i\omega l_c/V} e^{-2i\omega (l_t+l_c)/V} \right\}^T \sqrt{S_{rr}(\omega)}. \tag{18}$$

The relative position of the carriage and the track remains unchanged, and the track irregularity spectrum moves along the rail at the speed of the vehicle, generating displacement excitation between the wheel and the rail. The wheel-rail force can be computed as follows:

$$\mathbf{P} = -\left(\beta_\omega + \beta^{TB} + I_{4\times4}\beta^c\right)^{-1} \mathbf{R}(\omega). \tag{19}$$

Combining (19) with (2) and (15), the displacements of vehicle, track, and viaduct can be obtained. Through the displacement response $Z(\omega)$, the acceleration is further derived, and the acceleration response follows

$$a(\omega) = -\omega^2 \times Z(\omega), \tag{20}$$

where $a(\omega)$ and $Z(\omega)$ mean the acceleration and displacement, respectively.

3. Viscoelasticity Characterization of Underrail Rubber Pad

Mathematical model is usually used to characterize the dynamic viscoelasticity of the viscoelastic damping material. This study applies the constant frequency but variable temperature test method to obtain the measured data in order to expand to high frequency domain via temperature-frequency equivalence. The Temperature-Frequency Dependent Viscoelastic (TFDV) model is applied to characterize the dynamic mechanical properties of the underrail rubber pads.

3.1. Temperature-Frequency Equivalence.
For certain temperature range, most viscoelastic damping materials share the same dynamic mechanical characteristics between the low temperature condition and high frequency condition. Such temperature-frequency conversion relationship is so-called the Time-Temperature Equivalence (TTE) [23]. This gives the possibility of obtaining the high frequency dynamic mechanical characteristics of the viscoelastic damping materials at low temperature rather than at high frequency, which is arduous for most instruments. The TTE follows

$$E_e(\omega, T) = \frac{\rho T}{\rho_s T_s} E_e(\alpha_T \omega, T_s), \tag{21}$$

$$E_l(\omega, T) = \frac{\rho T}{\rho_s T_s} E_l(\alpha_T \omega, T_s), \tag{22}$$

where T_s means the reference temperature value, T means the measured temperature, $E_e(\omega, T)$ means the energy storage modulus, $E_l(\omega, T)$ represents the energy consumption modulus, ω denotes the excitation circular frequency, and α_T indicates the transferring factor [23].

3.2. FVMP Model.
The fraction Voigt and Maxwell mode in parallel (FVMP) model is a high-order fractional derivative model, which can accurately describe the dynamic mechanical characteristics of various mechanical parameters of the underrail cushion in a certain frequency band. Its time domain constitutive equation [24] follows

$$\frac{c_2}{\eta_1}\sigma(t) + \frac{1}{\eta_1}D^\alpha\sigma(t) = D^{\alpha+\gamma}\varepsilon(t) + c_1 D^\alpha\varepsilon(t) + \frac{\mu_2}{\eta_1}D^\beta\varepsilon(t) + c_2 D^\gamma\varepsilon(t) + c_1 c_2\varepsilon(t), \tag{23}$$

where $c_1 = \mu_1/\eta_1$ and $c_2 = \mu_2/\eta_2$. μ_1 and μ_2 mean the elastic parameters of the FVMP model, η_1 and η_2 represent the viscosity parameters of the FVMP model, and α, β, and γ indicate the fractional derivative order.

After transforming and separating (23), the storage modulus, dissipation modulus, and loss factor are obtained as

$$E_s(\omega) = \mu_1 + \eta_1\omega^\gamma \cos\frac{\gamma\pi}{2} + \mu_2\frac{\omega^{\alpha+\beta}\cos(((\beta-\alpha)/2)\pi) + c_2\omega^\beta\cos((\beta/2)\pi)}{(c_2)^2 + \omega^{2\alpha} + 2c_2\omega^\alpha\cos((\alpha/2)\pi)}, \tag{24}$$

$$E_l(\omega) = \eta_1\omega^\gamma \sin\frac{\gamma\pi}{2} + \mu_2\frac{\omega^{\alpha+\beta}\sin(((\beta-\alpha)/2)\pi) + c_2\omega^\beta\sin((\beta/2)\pi)}{(c_2)^2 + \omega^{2\alpha} + 2c_2\omega^\alpha\cos((\alpha/2)\pi)}, \tag{25}$$

$$\tan\delta = \frac{E_l}{E_s}. \tag{26}$$

3.3. TFDV (Temperature Frequency Dynamic Viscoelastic) Model. This study tries to establish a comprehensive dynamic model with considering both temperature variation and frequency variation simultaneously to analyze the concurrent effect of vibration frequency and ambient

temperature. The TTE is introduced to the FVMP model firstly, and substituting (21) and (22) into (24) and (25), respectively, leads to the temperature-frequency variation model as

$$E_s(\omega, T) = \frac{\rho T}{\rho_s T_s}\left(\mu_1 + \eta_1\omega_T^\gamma \cos\frac{\gamma\pi}{2} + \mu_2\frac{\omega_T^{\alpha+\beta}\cos(((\beta-\alpha)/2)\pi) + c_2\omega_T^\beta\cos((\beta/2)\pi)}{(c_2)^2 + \omega_T^{2\alpha} + 2c_2\omega_T^\alpha\cos((\alpha/2)\pi)}\right),$$

$$E_l(\omega, T) = \frac{\rho T}{\rho_s T_s}\left(\eta_1\omega_T^\gamma \sin\frac{\gamma\pi}{2} + \mu_2\frac{\omega_T^{\alpha+\beta}\sin(((\beta-\alpha)/2)\pi) + c_2\omega_T^\beta\sin((\beta/2)\pi)}{(c_2)^2 + \omega_T^{2\alpha} + 2c_2\omega_T^\alpha\cos((\alpha/2)\pi)}\right), \tag{27}$$

$$\tan\delta(\omega, T) = \frac{E_l(\omega, T)}{E_s(\omega, T)},$$

where $\omega_T = \alpha_T\omega$.

The schematic diagram of the constitutive model (TFDV model) for the underrail rubber pad established in this study is shown in Figure 4.

3.4. Temperature Variant Mechanical Test of Underrail Rubber Pad. The stiffness and damping of the under-rail rubber pad account for about 95% of the fastener system, so the stiffness and damping of the underrail rubber pad can be considered as the mechanical parameters of the fastener system [25]. Underrail rubber pad mainly provides the dynamic stiffness and loss factor of fasteners. The test object in this paper is the underrail rubber pad in the HSR WJ-7B constant resistance fastener system, as shown in Figure 5.

The test uses the EPLEXOR 500N Dynamic Thermomechanical Analyzer (DMA, as shown in Figure 6) produced by the German GABO Company for compression test.

The sample is a cylinder ø15 mm × ø10 mm, the excitation frequency is 2 Hz, the static strain is controlled at 1.0%, the dynamic strain is controlled at 0.1%, and the temperature control system is used to adjust the test environment temperature from −60°C to 40°C, extract the test

values of modulus and loss factor at this time, and finally get the temperature spectrum of the underrail rubber pad, as shown in Figure 7.

3.5. Dynamic Characteristics of Underrail Rubber Pads

3.5.1. Temperature Variant Dynamic Characteristics of Underrail Rubber Pad. There are three forms of viscoelastic damping materials at different temperatures: glassy, rubbery, and viscous flow. As the temperature changes, the corresponding mechanical parameters of viscoelastic damping materials will also change in different forms accordingly. Figure 7 shows the DMA test results of the underrail rubber pad in the range [−60, 40]°C.

In Figure 7, at low temperatures, the underrail rubber pad behaves in a glassy state, its storage modulus value is large and slowly decreases with the increase of temperature, and its energy dissipation modulus increases with the increase of temperature; when the temperature rises, the material is in the glass transition zone; in this temperature range, the storage modulus decreases sharply, and the energy dissipation modulus decreases sharply as the temperature
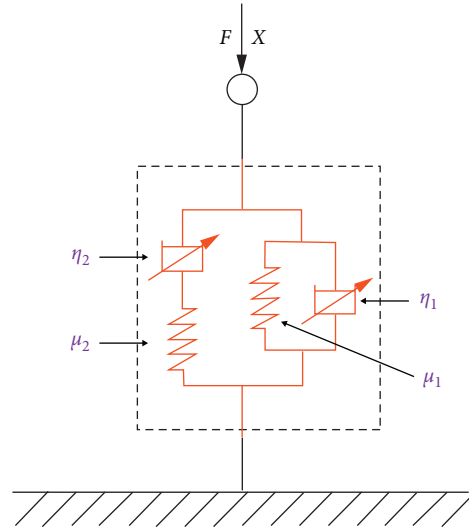
FIGURE 4: Schematic diagram of the TFDV model of rubber pad under rail.
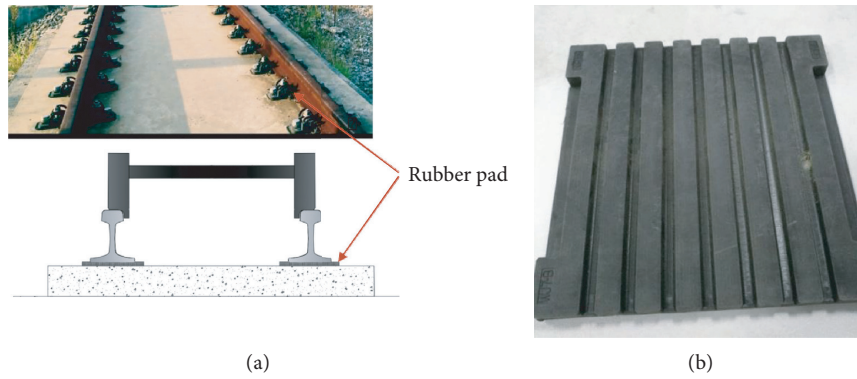

(a)

(b)

FIGURE 5: WJ-7B fastener system: (a) rail fastener system; (b) underrail rubber pad.

increases after reaching the peak temperature of the energy dissipation modulus ($-50.7°C$). When the temperature rises to a certain range, the modulus value of the rubber pad under the rail tends to be stable, and this state is in a rubber state.

The loss factor of the rubber pad under the rail has a peak at the glass transition temperature T_g ($-45.7°C$). When the temperature is less than T_g, the loss factor increases sharply with the increase in temperature. When the temperature is greater than T_g, the loss factor decreases sharply and the rate of decrease gradually slows down. When the temperature rises to a certain range, the value of the loss factor tends to stabilize. The glass transition temperature T_g ($-45.7°C$) of the underrail rubber pad obtained from the test data and the corresponding loss factor are 0.55.

In a certain temperature range, the temperature change test value of the underrail rubber pad shows obvious low-temperature sensitivity and high-temperature stability. Under low-temperature conditions, the mechanical properties of the underrail rubber pad have direct correlation with change to the mechanical response of the vehicle, track, and bridge subsystems.

3.5.2. Frequency-Varying Dynamic Characteristics of the Underrail Rubber Pad

(1) Temperature-Frequency Equivalence. To obtain the frequency-varying viscoelastic dynamic characteristics, combining the DMA temperature sweep test and the principle of temperature-frequency equivalence, the dynamic performance of the underrail rubber pad can be obtained. The frequency-varying mechanical characteristics of the under rail rubber pad when the reference temperature is $20°C$ is taken as an example. Figure 8 shows the frequency-dependent modulus value and loss factor after temperature-frequency equivalent treatment when the reference temperature of the underrail rubber pad is $20°C$.

(2) Frequency Domain Data Model Fitting. To ensure the fitting accuracy of the multiobjective function to the data, the frequency domain discrete data obtained in (1) is fitted with the high-order fractional derivative FVMP model, and the FVMP model parameters are identified in combination with the genetic algorithm. Model parameters are shown in Table 1. To verify the fitting effect of the model, this paper

FIGURE 6: Dynamic thermomechanical analyzer.

(a)

(b)
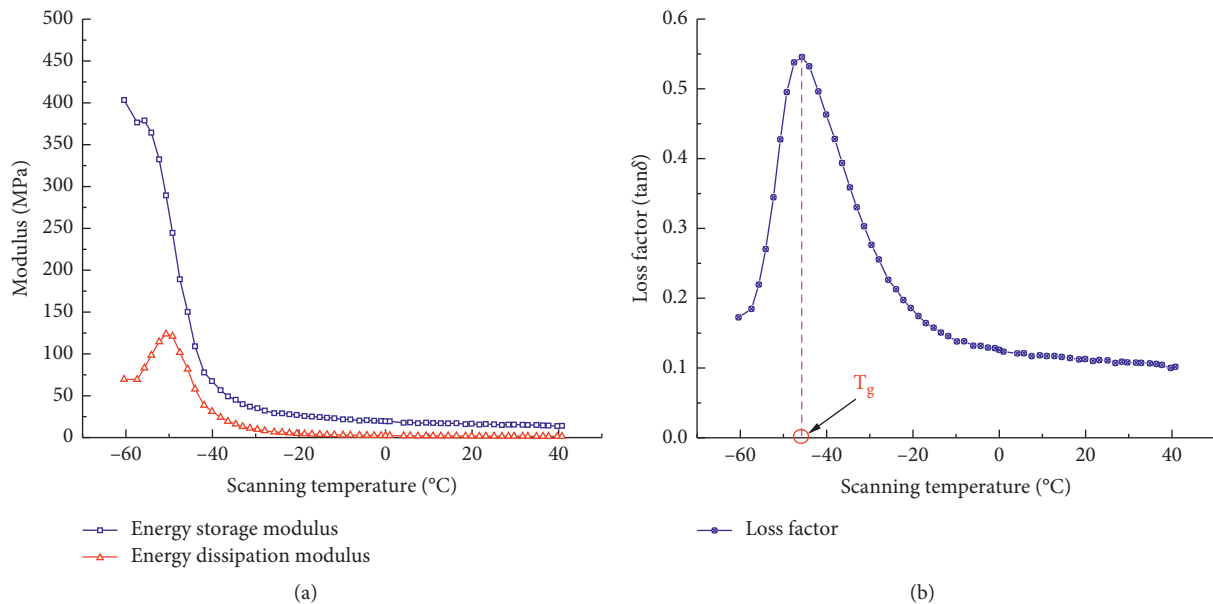
FIGURE 7: DMA test of rubber pad: (a) modulus; (b) loss factor.

compares the frequency-domain discrete dynamic parameter data of the undertrack rubber pad with the fitting curve of the FVMP model, shown in Figure 8.

Figure 8 shows the comparison between the test values of the modulus value and loss factor of the underrail rubber pad and the fitting curve of the FVMP parameter model. In Figure 8(a), both the modulus value and loss factor of the underrail rubber pad increase with the increase in frequency and increase of amplitude gradually slows down. In Figure 8(b), the frequency domain discrete dynamic

FIGURE 8: Comparison of fitted data and the tested data for the rubber pad: (a) modulus; (b) loss factor.

TABLE 1: Model parameters of underrail rubber pads.

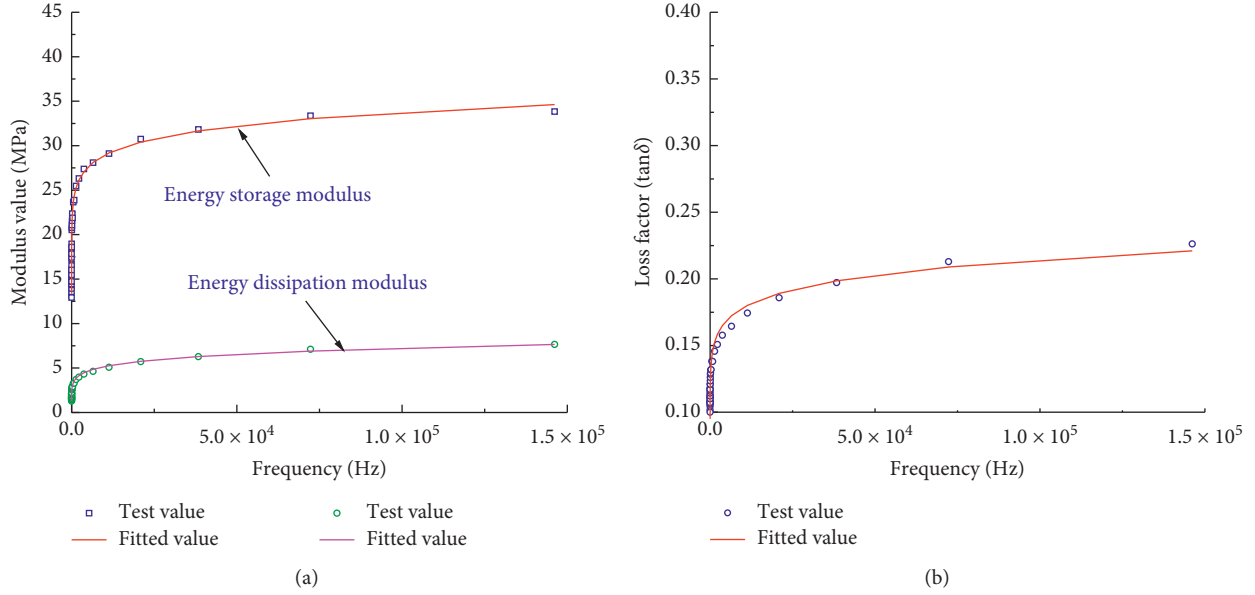| Parameter	Energy storage modulus model	Energy consumption modulus
μ_1	0.008	—
η_1	0.004	2.757
μ_2	59.672	0.001
η_2	17.537	0.001
α	0.041	1.754
β	0.08	2.813
γ	0.232	0.216

parameter values of the underrail rubber pad are compared with the FVMP parameter model simulation value. The FVMP parameter model can better describe the frequency change trend of its modulus value and loss factor, indicating that the FVMP model can accurately reflect frequency variation characteristics of rubber pads under derailment.

3.5.3. Characterization of Underrail Rubber Pad via the TFDV Model. Based on the TFDV model, the temperature variation $(-30, -20)°$C test data of the underrail rubber pad is processed; combined with the FVMP model parameters identified by the genetic algorithm, the three-dimensional dynamics of the temperature-frequency variation of the underrail rubber pad's storage modulus and loss factor can be obtained; see Figure 9.

In Figure 9, the storage modulus value and loss factor of the underrail rubber pad characterized by the TFDV model show a curved relationship with the frequency-temperature change; within a certain frequency/temperature range, the storage modulus value of the underrail rubber pad and the loss factor increase with decreasing temperature and increasing frequency. The dynamic parameters of underrail rubber pads have obvious temperature and frequency dependence, and the influence of low temperature on the dynamic parameters is more significant—the energy storage

of underrail rubber pads. The dynamic properties of modulus viscoelasticity illustrate the characteristics of underrail rubber pads being rigid at low temperature/high frequency and soft at high temperature/low frequency.

4. Viscoelastic Effect of the Undertrack Rubber Pad on the Vehicle-Track-Bridge System

4.1. Computation Condition. The computation condition is illustrated in Tables 2 and 3.

The track irregularity adopts the German spectrum (wavelength [1, 100] m), shown in Figure 10, the low-frequency dynamic response of the vehicle-rail-bridge system can be calculated, and when the Sato spectrum (wavelength < 1 m) is used as short-wave irregularity spectrum, the high-frequency dynamic response of the vehicle-rail-bridge system can be computed; this study uses the German low interference spectrum and the Sato spectrum as the track irregularity excitation [26].

In terms of German spectral density function, it is defined as

$$S_v(\omega) = \frac{A_v \omega_c^2}{\left(\omega^2 + \omega_r^2\right)\left(\omega^2 + \omega_s^2\right)} \left(\text{m}^2/\text{rad/m}\right), \qquad (28)$$
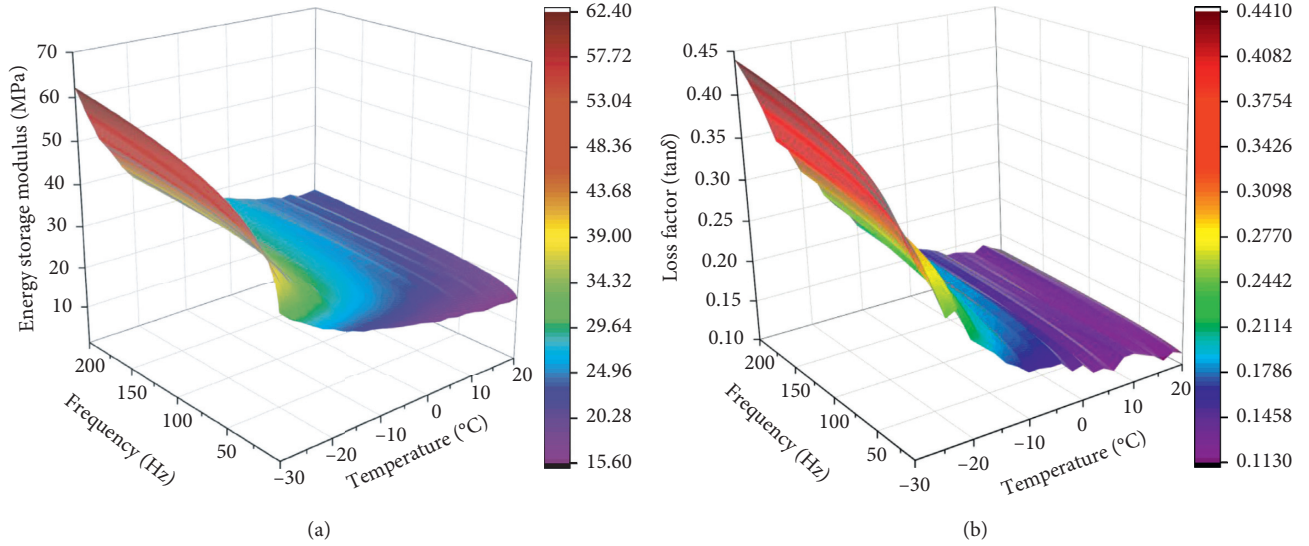
Figure 9: Three-dimensional diagram of viscoelastic dynamic characteristics of rubber pad under rail: (a) energy storage modulus; (b) loss factor.

Table 2: Parameters of CRH380A high-speed train.

Parameters	Values
Rated load car body mass (kg)	42934
Bogie mass (kg)	3300
Wheelset mass (kg)	1780
Moment of inertia of car body nodding (kg·m^2)	1.712×106
Bogie nodding moment of inertia (kg·m^2)	1807
Vertical stiffness of primary suspension (N·m^{-1})	1.176×106
Primary suspension damping (N·s/m)	1.0×104
Secondary suspension stiffness (N·m^{-1})	2.4×105
Secondary suspension damping (N·s/m)	2.0×104
Car length (m)	25
Vehicle distance (m)	17.5
Fixed wheelbase (m)	2.5

where the low interference spectrum is used, and the parameters are $A_v = 4.032e-7$ m·rad, $\omega_c = 0.8246$ rad/m, $\omega_r = 0.0206$ rad/m, and $\omega_s = 0.4380$ rad/m.

Sato spectral density is defined as

$$S(\omega) = \frac{A}{\omega^{-n}} \left(m^2/rad/m \right), \tag{29}$$

where the surface of the track is in good condition, $A = 0.065$, and $N = 3.06$.

4.2. Results Analysis. The influence of the frequency variation parameters of the underrail rubber pads on the dynamic response of the vehicle-rail-bridge coupling system at ambient temperatures of 20°C, −20°C, and −30°C is used, shown in Table 4. According to the storage modulus of the underrail rubber pads measured by the DMA test and the external dimensions of the test material, the energy storage stiffness and loss factor temperature change values of the underrail rubber pads at different temperatures can be

converted, and the corresponding temperature-frequency equivalent treatment can be used to obtain the frequency change data.

4.2.1. Viscoelastic Effect of the Underrail Rubber Pad on the Dynamic Flexibility. To analyze the influence of the viscoelastic dynamic characteristics of the underrail rubber pad on the dynamic flexibility of the vehicle-track-bridge system, it is necessary to analyze the dynamic flexibility of the vehicle-rail-bridge coupling system and the rail-bridge under the temperature change characteristics of the underrail rubber pad—the longitudinal attenuation rate of the system. Load the unit simple harmonic force on the wheel, and the obtained wheel displacement is the wheel dynamic flexibility; when the unit simple harmonic force is loaded on the rail; the obtained rail-bridge system displacement is the rail-bridge system dynamic flexibility.

(1) Vehicle-Rail-Bridge Dynamic Flexibility Amplitude and Phase. Based on the obvious vibration response of the wheel-rail contact position, this paper analyzes the system dynamic flexibility of the first wheel-rail contact position. Under the frequency change conditions of the rubber pads under different ambient temperatures, the dynamic flexibility amplitude and phase of the vehicle-rail-bridge system are shown in Figures 11–14.

From Figures 11–13, the dynamic flexibility of the wheel is the largest at 1 Hz, which corresponds to the natural frequency of the vehicle's secondary suspension. In the frequency range [1, 200] Hz, the dynamic flexibility of the wheel gradually decreases with the increase of frequency; the dynamic flexibility of the contact spring is considered as constant; the peak value of rail-bridge dynamic flexibility at 5 Hz corresponds to the first-order natural frequency of the bridge-bearing system.

TABLE 3: Dynamic parameters of track-bridge structure.

| Components	Item/symbol/unit	Values
Rail	Elastic modulus (N/m^2)	2.1 e11
	Moment of inertia of section (m^4)	$3.217e-5$
	Density (kg/m^3)	7850
	Sectional area (m^2)	$7.745e-3$
	Shear modulus (N/m^2)	$7.7e10$
	Section factor (κ)	0.4
	Loss factor (η_r)	0.01
	Stiffness (MN/m)	Temperature/frequency variant
Fastener	Loss factor	Temperature/frequency variant
	Fastener space (m)	0.625
	Elastic modulus (N/m^2)	$3.6e10$
	Moment of inertia of section (m^4)	$1.7e-3$
Slab	Density (kg/m^3)	2500
	Sectional area (m^2)	0.51
	Loss factor	0.1
	Stiffness (N/m)	$3.79e11$
CA mortar	Loss factor	0.2
	Elastic modulus (N/m^2)	$3.0e10$
	Moment of inertia of section (m^4)	$7.3125e-3$
Base plate	Density (kg/m^3)	2500
	Sectional area (m^2)	0.975
	Loss factor	0.1
	Stiffness (N/m)	$2.1e11$
Slipping layer	Loss factor	0.2
	Length (m)	32
	Elastic modulus (N/m^2)	$3.6e10$
	Moment of inertia of section (m^4)	11.056
Viaduct	Density (kg/m^3)	2650
	Sectional area (m^2)	9.089
	Loss factor	0.1
	Stiffness (N/m)	$6e9$
Viaduct bearing	Bearing spatial interval (m)	32
	Loss factor	0.25
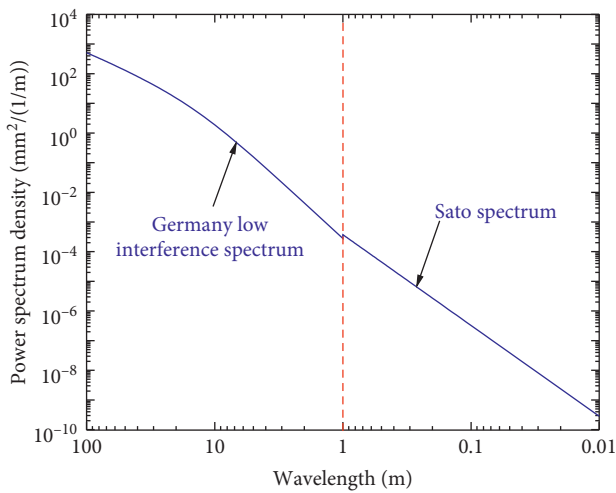
FIGURE 10: Irregularity spectrum.

In Figure 11, the total dynamic flexibility in the frequency band below 25 Hz is mainly affected by the wheels. The total dynamic flexibility in the frequency band [25, 120] Hz is mainly determined by the wheel and track-bridge dynamic flexibility. The total dynamic flexibility appears at a minimum value at 59 Hz. The total dynamic flexibility in the frequency band [120, 200] Hz is mainly affected by the track-bridge dynamic flexibility.

In Figure 12, the total dynamic flexibility in the frequency band below 30 Hz is mainly affected by the dynamic flexibility of the wheels. The total dynamic flexibility in the frequency band [30, 150] Hz is mainly determined by the dynamic flexibility of the wheels and the rail-bridge. The total dynamic flexibility appears extremely small at 75 Hz. The total dynamic flexibility in the frequency band [150, 200] Hz is mainly affected by the track-bridge dynamic flexibility.

In Figure 13, the total dynamic compliance in the frequency range below 40 Hz is mainly affected by the wheels. The total dynamic compliance in the frequency range [40, 170] Hz is mainly determined by the wheel and track-bridge dynamic compliance. The total dynamic compliance appears at a minimum at 93 Hz. The total dynamic compliance of the frequency band [170, 200] Hz is mainly affected by the track-bridge dynamic compliance; The amplitudes of the dynamic compliances of the wheel and the track-bridge at the

TABLE 4: Temperature/frequency characteristic calculation conditions.

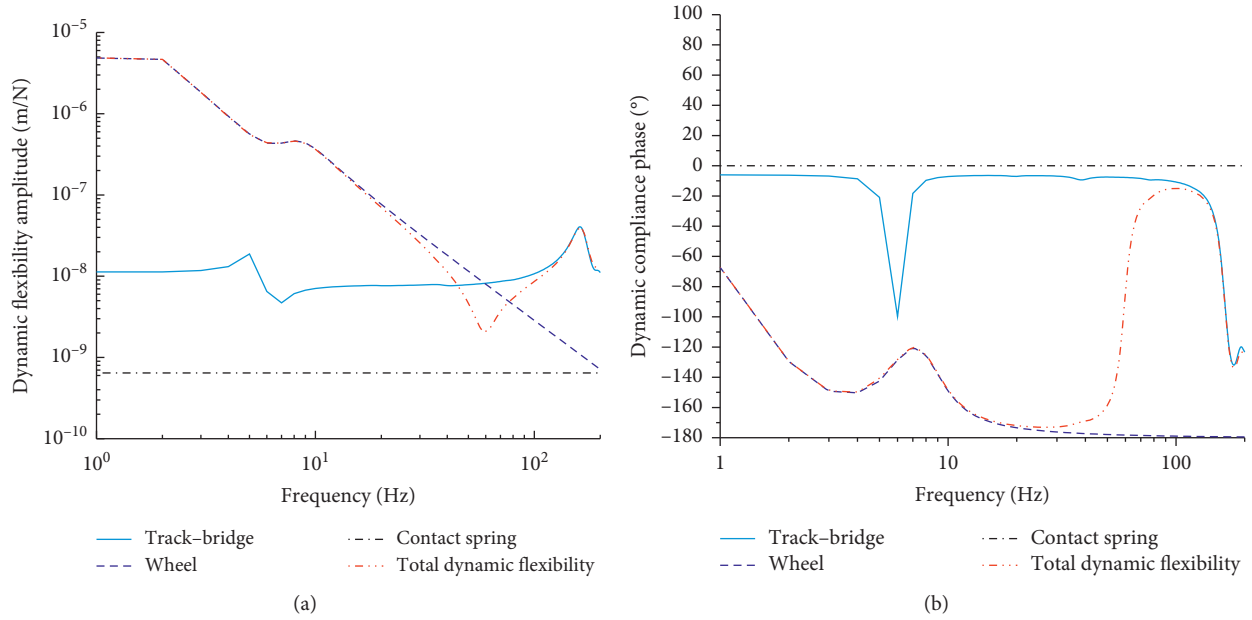| Material type	Ambient temperature (°C)	Energy storage modulus kN/m	Loss factor
WJ-7B fastener	20 −20 −30	Frequency variant	Frequency variant

FIGURE 11: Dynamic compliance amplitude and phase of vehicle-track-bridge system with rubber pad at 20°C: (a) amplitude; (b) phase.
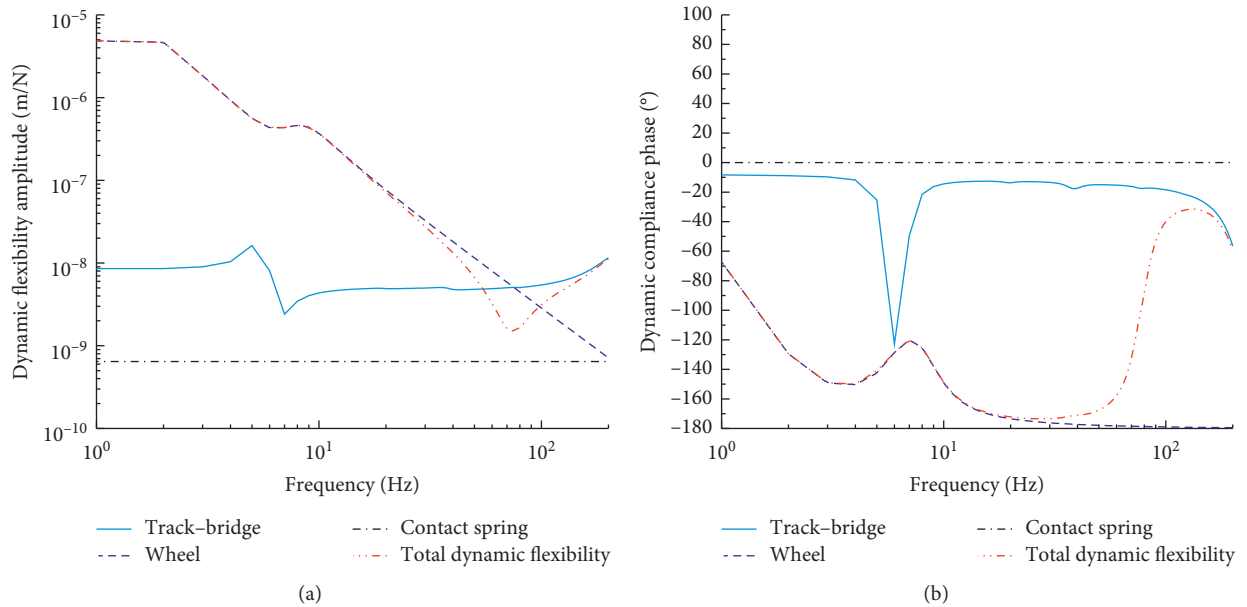

FIGURE 12: Dynamic compliance amplitude and phase of vehicle-track-bridge system with constant resistance elastic pad at −20°C: (a) amplitude; (b) phase.
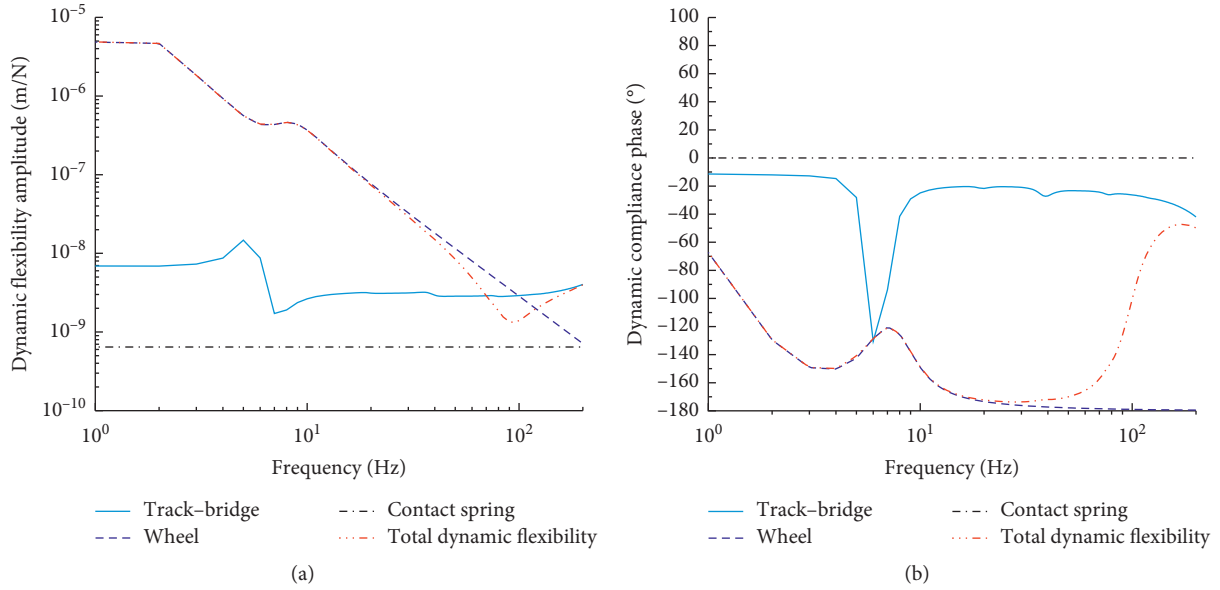
FIGURE 13: Dynamic compliance amplitude and phase of vehicle-track-bridge system with constant resistance elastic pad at −30°C: (a) amplitude; (b) phase.

frequency corresponding to the minimum point of the total dynamic compliance are equal, and phases are opposite; this frequency point is the natural frequency of the rail-bridge system.

In Figure 14, the total dynamic compliance amplitude curve and phase curve at different temperatures basically coincide in the frequency band below 25 Hz. This is because the total dynamic compliance in this frequency band is mainly determined by the wheel dynamic flexibility, and the viscoelasticity of the underrail rubber pad affects the wheel movement. The main frequency of the minimum point and the phase main frequency of the three total dynamic flexibility curves shift to high frequency with the decrease of temperature. This is because the lower the temperature, the greater the stiffness of the rubber pad under the rail, which leads the overall rigidity of the rail-bridge system to be larger.

(2) Track Decay Rate (TDR) of Track-Bridge System. The unit simple harmonic force is applied at wheel-rail contact point 1, and the response at wheel-rail contact point 3 is called the transmission dynamic flexibility between wheel-rail contact points 1 and 3. This section uses the transmission dynamic compliance decay rate to describe the track-viaduct relation, i.e., the relation between the dynamic flexibility of the bridge origin and the dynamic flexibility of the span; the TDR of the structure [27] is expressed as

$$\Lambda = \frac{20\lg\left(|z_0|/|z_i|\right)}{L},$$ (30)

where z_0 is the displacement of contact point 1 when unit simple harmonic force is applied at wheel-rail contact point 1 and z_i is the displacement of contact point 3 when unit simple harmonic force is applied at wheel-rail contact point 1.

Figure 15 shows the TDR of the track-bridge system under the temperature/frequency change conditions of the undertrack rubber pad.

In Figure 15, in the frequency range [0, 122] Hz, the TDR of the track-bridge system decreases with the decrease of temperature; that is, the decrease in temperature in this frequency band increases the longitudinal transmission of vibration along the track-bridge system, which leads to vibration due to energy conservation. The vertical transmission along the track-bridge system is reduced; in the frequency range [181, 200] Hz, the TDR of the track-bridge system increases with the decrease of temperature; that is, the decrease in temperature in this frequency band causes the vibration to travel along the track-bridge system, while longitudinal transmission decreases. Due to the conservation of energy, the vertical transmission of vibration along the track-bridge system increases; the change trend of the TDR spectrogram of the track-bridge system at different temperatures is basically the same.

To summarize, the viscoelasticity of the underrail rubber pad has a certain effect on the total dynamic flexibility and the TDR of the rail-bridge system. The lower the temperature, the smaller the minimum value of the total dynamic flexibility, and the frequency of the minimum value of the total dynamic flexibility will shift to high frequency. This is due to the increase in the stiffness of the rubber pad under the rail due to the decrease in temperature, which causes the overall track-bridge system stiffness increases; in the low frequency band, the decrease in temperature causes the TDR of the track-bridge system to decrease; that is, the longitudinal transmission of vibration along the track-bridge system increases and the vertical transmission decreases; in the higher frequency band, the temperature decrease causes the decay rate of vibration transmission of the track-bridge system to increase; that is,
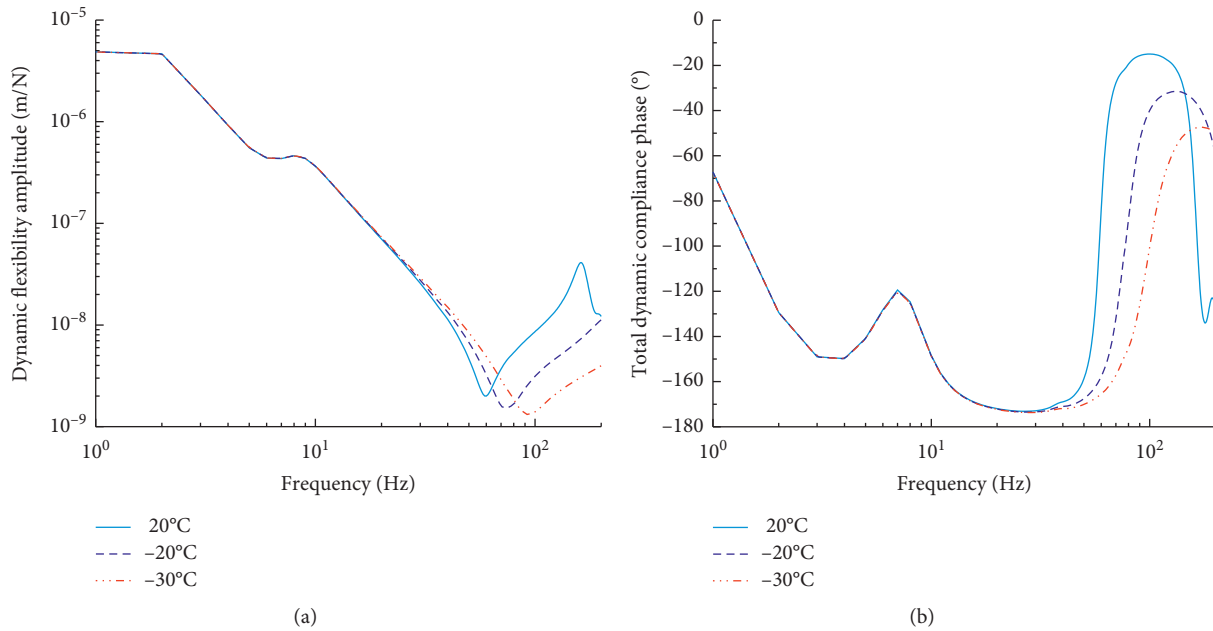
FIGURE 14: Amplitude and phase of total dynamic flexibility of rubber cushion car-rail-bridge system under different temperatures: (a) amplitude; (b) phase.
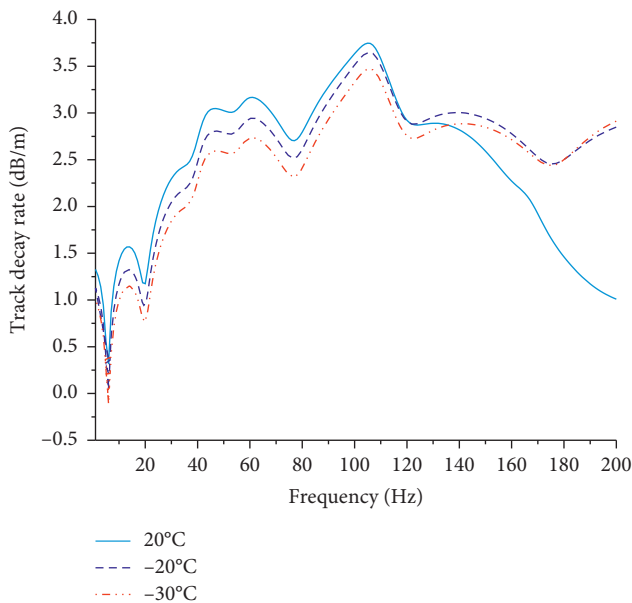

FIGURE 15: TDR of the track-bridge system.

the longitudinal transmission of vibration along the track-bridge system decreases and the vertical transmission increases.

4.2.2. Viscoelastic Effect of the Rubber Pad on the Random Vibration of the Vehicle-Track-Bridge System. This section uses virtual excitation method to calculate the random dynamic response of the vehicle-rail-bridge system at a speed of 350 km/h.

(1) Vertical Wheel-Rail Force. Figure 16 shows the wheel-rail force spectrum of the underrail rubber pad at different temperatures. To accurately analyze the influence of the viscoelasticity of the underrail rubber pad on the wheel-rail force, the main peak value of the wheel-rail force and the corresponding peak frequency in Figure 16 are extracted; see Table 5.

From Figure 16 and Table 5, the changing trend of the wheel-rail force amplitude calculated by the underrail rubber pad at different temperatures is consistent. Generally speaking, there is basically no difference in the wheel-rail force calculated in the frequency band below 25 Hz. The difference in the frequency range [25, 200] Hz is more obvious; the main peak frequency of the wheel-rail force amplitude curve is in the frequency range [55, 85] Hz, which is related to the coupled vibration of the wheel and the track-bridge; the stiffness of the rubber pad under the track decreases with the decrease of temperature. Therefore, the peak frequency corresponding to the main peak of the wheel-rail force shifts to high frequency, which shows that the amplitude of the high-frequency wheel-rail force increases with the decrease of temperature.

(2) Vehicle Body Vibration Acceleration Power Spectral Density. Figure 17 shows the acceleration PSD of car body nodding and ups and downs of the underrail rubber pad at three temperatures.

Extract the peak value of the PSD of the vehicle body nodding and the ups and downs vibration acceleration in Figure 17 and the corresponding peak frequency; see Table 6.

In Figures 17(a) and 17(b), the vehicle body ups and downs/nodding acceleration power spectrum curves calculated under different ambient temperatures for
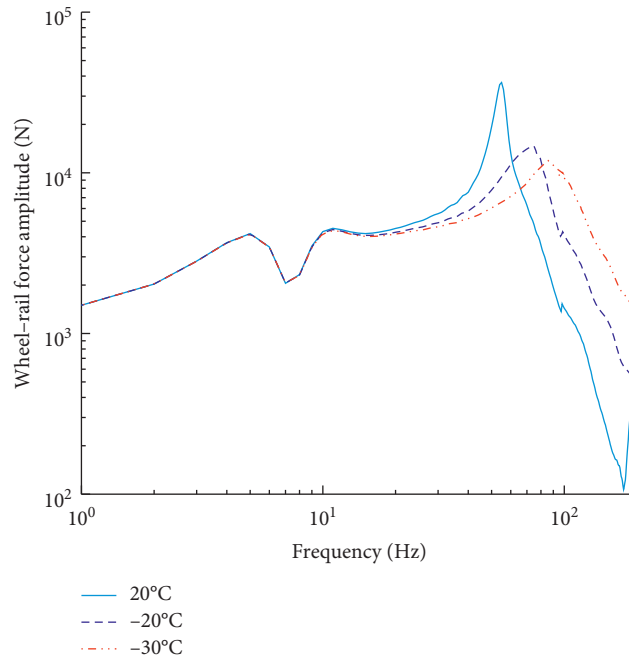
FIGURE 16: Wheel-rail force amplitude.

TABLE 5: Wheel-rail peak force and peak frequency.

Condition	Ambient temperature (°C)	Resonant frequency	
		Peak (N)	Frequency at peak (Hz)
Under rubber pad	20	3.646e4	55
	−20	1.470e4	75
	−30	1.203e4	85
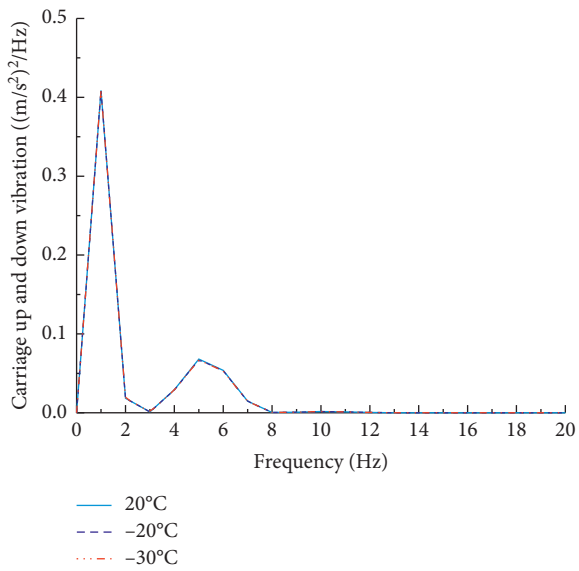
(a)
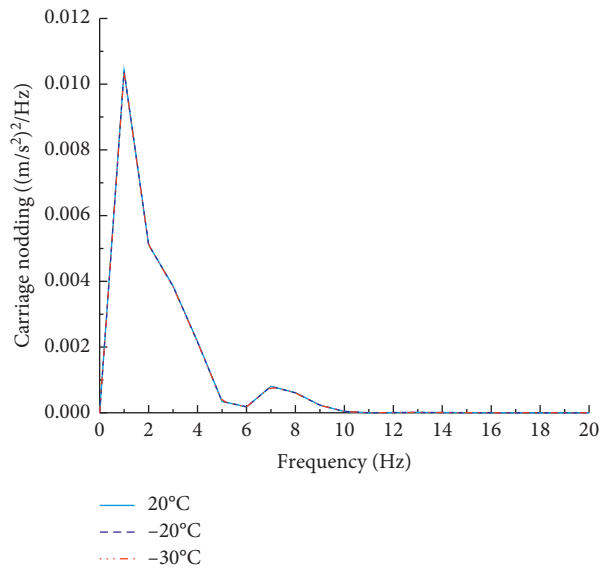
(b)

FIGURE 17: Power spectrum of vehicle body vibration acceleration when (a) carriage up and down vibration and (b) carriage nodding.

TABLE 6: Car body acceleration power spectrum peak and peak frequency.

Acceleration type	Ambient temperature (°C)	First resonant frequency		Second resonant frequency	
		Peak ((m/s²)²/Hz)	Frequency (Hz)	Peak ((m/s²)²/Hz)	Frequency (Hz)
Vehicle body ups and downs vibration acceleration	20	0.40840	1	0.06800	5
	−20	0.40860	1	0.06732	5
	−30	0.40870	1	0.06700	5
Vehicle body nodding vibration acceleration	20	0.01041	1	0.00081	7
	−20	0.01040	1	0.00080	7
	−30	0.01039	1	0.00079	7

underrail rubber pads basically overlap, mainly in the frequency band below 10 Hz; from Table 6, the vehicle body ups and downs vibration acceleration are in different working conditions. In this case, the calculated first main frequency is 1 Hz, the corresponding maximum peak value is $0.4087\,(m/s^2)^2/Hz$, the minimum peak value is $0.4084\,(m/s^2)^2/Hz$, and the difference between the two is only 0.07%. The second main frequencies are both 5 Hz, the corresponding maximum peak value is $0.06800\,(m/s^2)^2/Hz$, the minimum peak value is $0.06700\,(m/s^2)^2/Hz$, and the difference between the two is only 1.5%, which can be ignored; the car body nods. The first dominant frequency of vibration acceleration calculated under different working conditions is 1 Hz, the corresponding maximum peak value is $0.01041\,(m/s^2)^2/Hz$, the minimum peak value is $0.01039\,(m/s^2)^2/Hz$, and the difference between the two is only 0.2%; the second main frequency is 7 Hz, the corresponding maximum peak value is $0.0081\,(m/s^2)^2/Hz$, the minimum peak value is $0.0079\,(m/s^2)^2/Hz$, and the difference between the two is only 2.5%, which can be ignored and not counted; therefore, the viscoelastic dynamic characteristics of the underrail rubber pads have basically no effect on the dynamic response of the car body.

(3) Wheelset and Rail Vibration Acceleration Power Spectral Density. The dynamic response law of wheel-rail direct contact is similar. This article puts it together for analysis. Figure 18 shows the power spectral density of wheelset and rail vibration acceleration calculated under different temperatures for the rubber pad under the rail.

Extract the more obvious peaks and corresponding peak frequencies in the power spectrum of wheel sets and rails in Figure 18 and Tables 7 and 8.

From Figure 18(a) and Table 7, the power spectrum of wheelset acceleration of the underrail rubber pad at different ambient temperatures has no obvious difference within the frequency range of 25 Hz; the peak frequency is between 55 and 85 Hz; as the temperature decreases, the peak frequency of the wheelset acceleration power spectrum gradually

increases; in the low frequency band within 61 Hz, the lower the temperature, the smaller the amplitude of the wheelset vibration acceleration power spectrum; in the higher frequency band [81, 200] Hz, the higher the temperature, the lower the wheelset vibration acceleration power spectrum amplitude; this is similar to the wheel-rail force amplitude curve law.

From Figure 18(b) and Table 8, the power spectrum of rail vibration acceleration under different ambient temperatures has no obvious difference within the frequency range of 20 Hz; the peak frequency is between 55 and 98 Hz. As the temperature decreases, the peak frequency of the rail acceleration power spectrum curve gradually increases; in the low frequency stage within 66 Hz, the lower the temperature, the smaller the amplitude of the rail vibration acceleration power spectrum; in the [85, 200] Hz high frequency band, the lower the temperature, the higher the overall power spectral density of the vibration acceleration of the upper rail.

The viscoelastic dynamic characteristics of the under-rail rubber pad have an impact on the vehicle system and the random dynamic response of the rail. The viscoelasticity of the underrail rubber pad has almost no effect on the low-frequency acceleration PSD curve of the carriage body, wheel set, and rail because the dynamic response of the vehicle system and the rail and the total flexibility of the vehicle-rail-bridge system are closely related. In the low frequency band, the total dynamic flexibility is mainly determined by the wheel dynamic flexibility, while the viscoelasticity of the underrail rubber pad has no effect on the wheel dynamic flexibility; the viscoelasticity of the underrail rubber pad affects the wheel-rail force and the wheelset. The influence of certain rubber pad in the medium and high frequency range to the PSD of the rail is obvious. As the temperature decreases, the peak frequency of the PSD increases; in the lower frequency range, the lower the temperature is, the smaller the power spectrum amplitude will be; in the higher frequency band, the higher the temperature is, the greater the power spectrum amplitude will be.
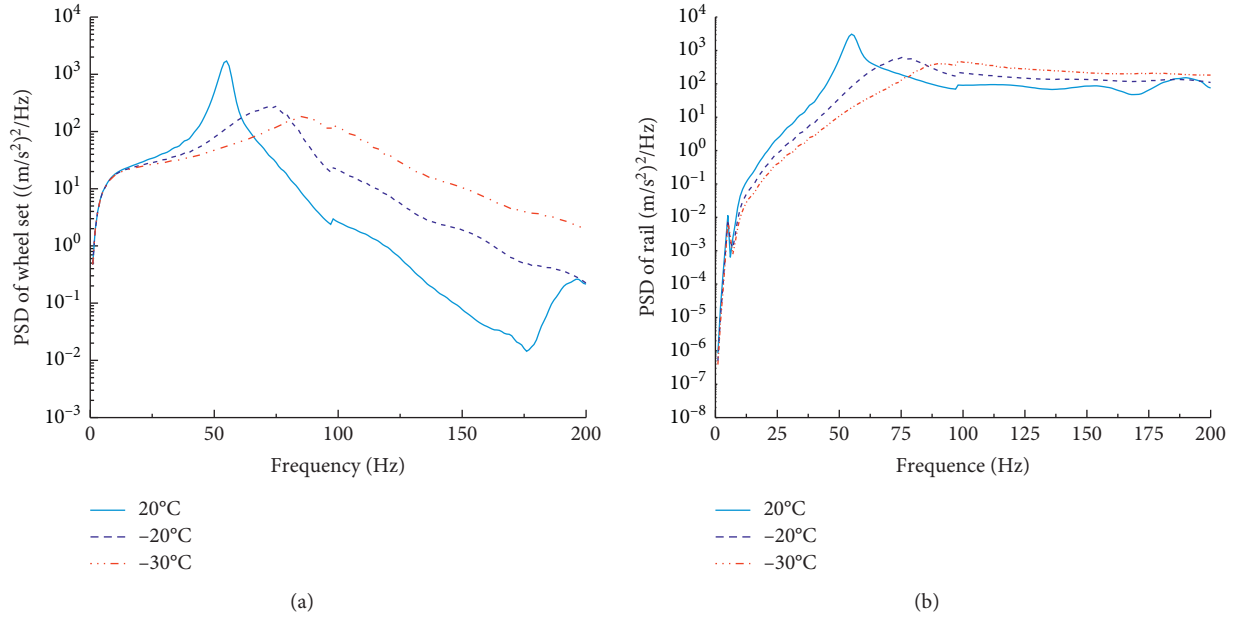
FIGURE 18: Power spectrum of temperature/frequency variable wheelset and rail acceleration of elastic cushion pad with constant resistance: (a) wheelset; (b) rail.

TABLE 7: Wheelset power spectrum peak and peak frequency.

Condition	Ambient temperature (^{o}C)	Peak (($m/s^2)^2$/Hz)	Frequency (Hz)
	20	1703	55
Under the constant resistance rail pad	−20	275.6	75
	−30	184	85

TABLE 8: Power spectrum peak and peak frequency of the rail.

Condition	Ambient temperature ($^{\circ}$C)	Peak value (($m/s^2)^2$/Hz)	Frequency (Hz)
	20	3074	55
Under the constant resistance rail pad	−20	625.7	75
	−30	473.8	98

5. Conclusions

This paper combines the TFDV model of the underrail rubber pad and the vehicle-track-bridge vertical coupling frequency domain analysis model, which uses the German spectrum and the Sato spectrum as the track irregularity. The conclusions are summarized as follows:

(1) The temperature change test value of the underrail rubber pad shows obvious low-temperature sensitivity and high-temperature stability within a certain temperature range; as to the storage of the underrail rubber pad characterized by the TFDV model, both the energy modulus value and the loss factor show a curved relationship with the frequency-temperature change; within a certain frequency/temperature range, the storage modulus value and loss factor of the underrail rubber pad both decrease with temperature and increase frequency.

(2) The lower the temperature is, the smaller the minimum value of the total dynamic flexibility will be; and the frequency of the minimum value of the total dynamic flexibility shifts to high frequency. In the low frequency band, the temperature decrease causes the TDR of the track-bridge system to decrease; that is, the longitudinal transmission of vibration along the track-bridge system increases, and the vertical transmission decreases; in the higher frequency band, the temperature decreases while the dynamic flexibility TDR of the track-bridge system increases; that is, the dynamic flexibility decreases along the track-bridge system's longitudinal transmission and increases the vertical transmission.

(3) The viscoelastic dynamic characteristics of the rubber pad have little effect on the amplitude of the power spectrum of the vehicle body vibration acceleration. Since the total flexibility of the vehicle-rail-bridge system is closely related to its dynamic

response, the wheels in the low frequency range mainly determine the total flexibility. The viscoelasticity of the rubber pad under the rail has no effect on the dynamic flexibility of the wheel; the primary and secondary suspension of the vehicle dissipate a large amount of low-frequency vibration energy transmitted to the car body.

(4) The viscoelastic dynamic characteristics of the underrail rubber pad have the same effect on the wheel-rail force, wheelset, and rail vibration acceleration power spectrum. As the temperature decreases, the peak frequency of the power spectrum curve gradually increases; in the lower frequency band, the lower the temperature is, the smaller the power spectrum amplitude will be; in the higher frequency band, the lower the temperature is, the greater the power spectrum amplitude will be. The viscoelasticity of the underrail rubber pad has a similar effect on the vibration of the track-bridge system. As the ambient temperature of the underrail rubber pad decreases, the dominant frequency band of the power spectrum curve shifts to high frequencies.

Data Availability

The data are available from the corresponding author upon request.

Conflicts of Interest

The authors declare that they have no conflicts of interest.

Acknowledgments

References

[1] X. Lei, *High Speed Railway Track Dynamics: Model, Algorithm and Application*, Science Press, Beijing China, 2015.

[2] Q. Peng, J. Li, Y. Yang et al., "Influence of high-speed railway construction on railway transportation of China," *Journal of Sothwest Jiaotang University*, vol. 51, no. 3, pp. 525–533, 2016.

[3] G. Zhou, D. Chen, F. Zhou, and K. Zhang, "Research on market share rate models of passenger transport competition between high-speed rail and road," *Journal of the China Railway Society*, vol. 42, no. 1, pp. 1–8, 2020.

[4] Z. Yu, H. He, L. Jiang et al., "Dynamics and key technology research on high-speed railway track-bridge system under multiple dynamic sources," *China Civil Engineering Journal*, vol. 50, no. 11, pp. 1–9, 2017.

[5] Z. Jin, S. Pei, and S. Qiang, "Study on derailment of railway vehicles on bridges during earthquakes based on IDA analysis," *China Civil Engineering Journal*, vol. 47, no. S1, pp. 234–239, 2014.

[6] L. Liu, Z. Zuo, Y. Zhou, and J. Qin, "Insights into the effect of WJ-7 fastener rubber pad to vehicle-rail-viaduct coupled dynamics," *Applied Science*, vol. 10, no. 5, 2020.

[7] D. J. Thompsom, *Railway Noise and Vibration; Mechanisms, Modeling and Means of Control*, Elsevier, Oxford, UK, 2009.

[8] L. Liu, J. Qin, Y.-L. Zhou, R. Xi, and S. Peng, "Structural noise mitigation for viaduct box girder using acoustic modal contribution analysis," *Structural Engineering and Mechanics*, vol. 72, no. 4, 2019.

[9] L. I. Qi and D. J. Wu, "Analysis of the dominant vibration frequencies of rail bridges for structure-borne noise using a power flow method," *Journal of Sound and Vibration*, vol. 332, pp. 4153–4163, 2013.

[10] B. Zhang, X. Lei, and Y. Luo, "Improved algorithm of iterative process for vehicle-track coupled system based on Newmark formulation," *Journal of Central South University (Science and Technology)*, vol. 47, no. 1, pp. 298–306, 2016.

[11] D. J. Thompson and J. W. Verheij, "The dynamic behaviour of rail fasteners at high frequencies," *Applied Acoustics*, vol. 52, no. 1, pp. 1–17, 1997.

[12] J. Maes, H. Sol, and P. Guillaume, "Measurements of the dynamic railpad properties," *Journal of Sound and Vibration*, vol. 293, no. 3–5, pp. 557–565, 2006.

[13] J. Yang, C. Maoru, M. Zhu et al., "The non-linear constitutive model of elastic rubber mat for rail vehicles," *Journal of Vibration Engineering*, vol. 29, no. 2, pp. 291–297, 2016.

[14] Z. Liu, *Study on the Influence of Amplitude-Dependent and Frequency-Dependent Dynamic Characteristics of Rubber Pads on Wheel-Rail Dynamic Response in High Speed*, Southwest Jiaotong University, Chengdu, China, 2017.

[15] Y. Zhao, Z. Hou, Y. Huang et al., "A fractional derivative model with five parameters for rubber materials," *Journal of Vibration and Shock*, vol. 34, no. 23, pp. 37–41, 2015.

[16] L. Liu, P. Lu, and J. Qin, "Random vibration analysis of vehicle-track coupling system based on fastener FVMP model," *Journal of the China Railway Society*, vol. 41, no. 5, pp. 93–100, 2019.

[17] Q. Yin, C. Cai, and S. Zhu, "Effect of frequency-dependent stiffness of rail fasteners on the wheel-rail vibration noise," *Journal of Vibration and Shock*, vol. 36, no. 18, pp. 231–237, 2017.

[18] P. Wang, Y. Fan, and W. Kai, "Symplectic model and its application of vertical environment vibration prediction about vehicle-track-tunnel coupled system," *Engineering Mechanics*, vol. 34, no. 5, pp. 171–178, 2017.

[19] W. Kai, Y. Fan, P. Wang, and W. Luo, "Symplectic random vibration analysis of vehicle-track coupled system considering frequency-dependent stiffness of rail pads," *Engineering Mechanics*, vol. 33, no. 9, pp. 123–130, 2016.

[20] Z. Zuo, L. Liu, J. Qin et al., "Analysis of influence of temperature variation characteristics of fastener rubber pads on vehicle-track vertical coupling dynamic responses," *Noise and Vibration Control*, vol. 40, no. 3, pp. 194–199, 2020.

[21] Z. Zhang, *Semi-analytic Analysis and Experimental Study of Ground Vibration Induced by Trains Moving over High-Speed Railway Bridges*, Southwest Jiaotong University, Chengdu, China, 2016.

[22] J. Yang, *Study on Prediction of High Speed Vehicle-Bridge Coupling Vibration and Viaduct Bridge Structure Noise Radiation*, Lanzhou Jiaotong University, Lanzhou, China, 2015.

[23] G. Chang, *Viscoelastic Damping Materials*, National Defense Industry Press, Beijing, China, 2012.

[24] Y. Zhao and Z. Hou, "Two viscoelastic constitutive models of rubber materials using fractional derivations," *Journal of*

Tsinghua University (Natural Science Edition), vol. 53, no. 3, pp. 378–383, 2013.

[25] K. Wei, P. Wang, F. Yang, and J. Xiao, "Influence of frequency-dependent dynamic parameters of rail pads on environmental vibration induced by subways in a tunnel," *Transportation Research Board*, vol. 2476, no. 1, pp. 8–14, 2015.

[26] W. Zhai and H. Xia, *Train-Track-Bridge Dynamic Interaction Theory and Engineering Application*, Science Press, Beijing, China, 2011.

[27] H. Liu, *A Study on Modelling, Prediction and its Control of Wheel/Rail Rolling Noise in High Speed Railway*, Shanghai Jiaotong University, Shanghai, China, 2011.